

---

Unterschrift BetreuerIn



TECHNISCHE  
UNIVERSITÄT  
WIEN  
Vienna University of Technology

## DIPLOMARBEIT

# Simulation of Operating IV-VI Semiconductor Laser Chips for the Development of Continuous Wave VECSELs

ausgeführt am Institut für Angewandte Physik  
der Technischen Universität Wien

In Zusammenarbeit mit  
CAMLIN TECHNOLOGIES CH in Zürich

unter der Anleitung von

**Ao.Univ.Prof. Dipl.-Ing. Dr.techn. Martin Gröschl** (TU Wien)

**Dr. sc. ETH Zürich Ferdinand Felder** (Camlin Technologies CH)

durch

**Peter Gerges,**

Matrikelnummer: 01229024

21. März 2020

---

Unterschrift Student



Die approbierte gedruckte Originalversion dieser Diplomarbeit ist an der TU Wien Bibliothek verfügbar.  
The approved original version of this thesis is available in print at TU Wien Bibliothek.

**Abstract:** Many important industrial and natural gases have strong absorption lines in the mid-wavelength infrared range, where the Vertical External Cavity Surface Emitting Lasers (VECSELs) have been realized with IV-VI semiconductors based on lead chalcogenides. Camlin Technologies CH has already commercialized VECSELs in pulsed mode for gas detection applications and the next step is to develop VECSELs for continuous wave (CW) operation. A better understanding of the current laser's heat flux is necessary in order to achieve higher output power and longer pulse lengths towards CW operation.

The main goal of this thesis is the creation of a *COMSOL Multiphysics*<sup>®</sup> model to simulate the heat profiles of these lasers under different settings. This model helps to understand electronic and optical losses and allows the discovery of effective heat removal. A series of photoluminescence measurements with different laser chips will also be done within this thesis for comparison with post-processed simulation results to obtain the unknown but necessary simulation parameters.

**Abriss:** Viele interessante industrielle und natürliche Gase haben starke Absorptionslinien im mittleren Wellenlängeninfrarotbereich, wo die Vertical External Cavity Surface Emitting Lasers (VECSELS) mit IV-VI Halbleitern auf Basis von Bleichalkogeniden realisiert worden sind. Camlin Technologies CH hat schon VECSELS als Puls laser für Anwendungen in der Gas Detektion erfolgreich kommerzialisiert und der nächste Schritt ist die Entwicklung eines VECSELS als Dauerstrich laser (CW). Um höhere Ausgangsleistung und längere Impulslängen für den Dauerstrichbetrieb zu erreichen, ist es notwendig den Wärmefluss der jetzigen Laser besser zu verstehen.

Das Hauptziel dieser Arbeit ist die Erstellung eines *COMSOL Multiphysics*<sup>®</sup> Modells, um die Wärmeprofile dieser Laser unter verschiedenen Einstellungen zu simulieren. Dieses Modell hilft, elektronische und optische Verluste zu verstehen, und ermöglicht die Entdeckung einer effektiven Wärmeabfuhr. In dieser Arbeit wird auch eine Reihe von Photolumineszenzmessungen mit verschiedenen Laserchips durchgeführt und diese mit verarbeiteten Simulationsergebnissen verglichen, um die unbekannt, aber notwendigen Simulationsparameter zu erhalten.

# Contents

<b>1</b>	<b>Introduction and Motivation</b>	<b>5</b>
1.1	Objectives of this project . . . . .	6
<b>2</b>	<b>Theory</b>	<b>7</b>
2.1	Overview of Mid-Infrared semiconductor lasers . . . . .	7
2.1.1	Mid-IR Laser Diode and Interband Cascade Laser (ICL) . . . . .	7
2.1.2	Quantum Cascade Laser (QCL) . . . . .	8
2.2	VECSEL Based on IV-VI Semiconductors . . . . .	9
2.2.1	IV-VI Semiconductors and their Properties . . . . .	10
2.2.2	VECSEL Design . . . . .	15
2.3	Gas Detection . . . . .	17
<b>3</b>	<b>Measurement</b>	<b>18</b>
3.1	Experimental Setup . . . . .	18
3.2	Post Processing . . . . .	20
3.3	Measurement Results . . . . .	21
3.3.1	Special Measurements . . . . .	21
3.3.2	Photoluminescence Spectroscopy (PL) Results . . . . .	23
<b>4</b>	<b>Simulation: Heat profile in COMSOL Multiphysics®</b>	<b>25</b>
<b>5</b>	<b>Simulation: Emission spectrum in Octave</b>	<b>34</b>
5.1	Temperature distribution . . . . .	35
5.2	Broadening effect . . . . .	38
<b>6</b>	<b>Usage - How to Simulate and Compare in COMSOL and Octave</b>	<b>40</b>
6.1	Introduction . . . . .	40
6.2	Parameters for user input and computing in COMSOL . . . . .	40
6.3	Plots & data export in COMSOL and emission spectrum in Octave . . . . .	41
<b>7</b>	<b>Results and Discussion</b>	<b>47</b>
<b>8</b>	<b>Conclusion and Outlook</b>	<b>58</b>
	<b>References</b>	<b>59</b>

# 1 Introduction and Motivation

Gas detection is of great interest for a wide range of applications since the 19th century. Nowadays the identification and quantification of gaseous hydrocarbons is a key attribute of many industrial fields. They are used for fast detection of leaks for quality assurance, safety ensurer via detection of toxic or flammable gases, monitoring feed stocks and measuring key species in products or processes. In atmospheric science high sensitivity gas detectors are used to measure and understand the profile and pathways of different gas species, especially greenhouse gases.

Gas sensors based on optical absorption have gained a lot of attention in the past years because they offer fast responses, high gas specificity, and real time measurement. The Camlin group researches the development of Vertical External Cavity Surface Emitting Lasers (VECSEL) which are tunable with emission in the mid-infrared (Mid-IR) and are therefore suitable for detection of gaseous hydrocarbons.

This thesis was carried out during an internship at Camlin Technologies in Zurich and focuses on the development of VECSELs operating at Continuous Wave (CW). The benefits of CW laser emission is their flexibility for adapting to different spectroscopic techniques. They can be externally tuned for wide wavelength range, have higher power output stability and high average output powers.

Camlins VECSELs cover the analysis of C1 to C4 alkanes (methane, ethane, propane, and butanes) in gas mixtures used in the petrochemical industry. The variety of possible applications includes natural/biogas gas composition analysis, energy content measurement, fuel blending and control, optimization of power generation (fuel cells, gas turbines), and monitoring of hydrocarbon leaks at pipelines and refineries [GFH<sup>+</sup>06, BJF02, CS10]. VECSELs at Camlin are based on IV-VI semiconductors and have their wavelength range from 3.0  $\mu\text{m}$  to 4.5  $\mu\text{m}$ , which is an interesting range for gas spectroscopy [SJS<sup>+</sup>04]. Properties such as a direct band-gap and a low Auger-recombination rate make lead chalcogenides [FPK<sup>+</sup>98, RKF<sup>+</sup>09] fit for use as a gain material. These IV-VI semiconductors in combination with VECSELs also result in a favorable (as already stated in [RFFS14]) beam quality and an outstanding tuning range compared to current

Mid-IR lasers. On the other hand, relatively high excitation powers lead to a soaring heat generation by high energy absorption in the active region of the laser chip and cause non-radiative recombination processes. This heat problem prevents current devices from lasing in CW mode at room temperature.

A solution to this problem is not obvious and still requires intense research. To do so, it is necessary to gain a better understanding of the current laser's heat flux in order to achieve higher output power and longer pulse lengths towards CW operation. The main goal of this thesis is the creation of a *COMSOL Multiphysics*<sup>®</sup> model to simulate the heat profiles of these lasers under different settings. This model helps to understand electronic and optical losses and allows the discovery of an effective heat removal.

## 1.1 Objectives of this project

A clear insight into the above mentioned heat problem shall be made to achieve CW operation by:

- Implementation of the measurement setup as a model into the simulation program *COMSOL Multiphysics*<sup>®</sup>.
- Post processing the simulation results into an emission spectrum and complete several measurements on the setup to compare both kind of results.
- Interpretation of these comparisons to find fitting material parameters for the simulation model.

The use of this simulation model should result in:

- A deeper understanding of the underlying physics and its effects by measuring and simulating different setup options.
- A better view on the laser's heat management in order to find fitting solutions for the achievement of CW operation.
- A further development of the model could reduce the production process of these lasers by simulating the desired VECSEL design.

## 2 Theory

### 2.1 Overview of Mid-Infrared semiconductor lasers

In this chapter, the most interesting Mid-IR semiconductor technologies will be briefly presented. A more extensive review is very well covered by several other books [CBJ12, Kri07].

Laser emission can be obtained from interband transitions between conduction and valence bands of semiconductor nanostructures such as quantum wells (QWs) or dots (QDs), or from intersubband (or intraband) transitions between confined levels in semiconductor nanostructures. Mid-IR laser diodes and interband cascade lasers (ICLs) rely on interband transitions while quantum cascade lasers (QCLs) are based on intersubband transitions.

#### 2.1.1 Mid-IR Laser Diode and Interband Cascade Laser (ICL)

Within a bulk semiconductor crystal, electrons may occupy states in one of two continuous energy bands:

- the valence band, which is heavily populated with low energy electrons
- and the conduction band, which is lightly populated with high energy electrons

The two energy bands are separated by an energy band gap in which there are no permitted states available for electrons to occupy. Conventional semiconductor laser diodes (type I) generate light by a single photon being emitted when a high energy electron in the conduction band recombines with a hole in the valence band. The energy of the photon and hence the emission wavelength of laser diodes is therefore determined by the band gap of the material system used. See (a) in figure 2.1.

The key feature that enables the realization of cascading within an interband diode is the so-called "type II", or broken-gap, band alignment between two different material layers. Whereas in type I QWs both energy bands are confined within the same material layer, the multi layer system is type II because the conduction band minimum of one layer lies at a lower energy than the valence band maximum of the second layer. This arrangement makes it easy to re-inject electrons from the

valence band of one stage of the ICL into the conduction band of the next stage via simple elastic scattering. Therefore the energy of photons emitted by interband cascade lasers is also determined by the band offset at the well/barrier interface. See (c) in figure 2.1.

A problem specific to interband Mid-IR lasers is carrier loss induced by the so-called Auger effect where non-equilibrium electron-hole pairs recombine and transfer their energy and momentum to another particle (electron or hole) rather than emit a photon [FGE<sup>+</sup>95, Kri07]. This effect has for long been considered as the most limiting factor for the fabrication of Mid-IR lasers. Additionally, in semiconductor laser diodes, electrons and holes are annihilated after recombining across the band gap and can play no further part in photon generation.

### 2.1.2 Quantum Cascade Laser (QCL)

A QCL however consists of a periodic series of thin layers of varying material composition forming a superlattice. This superlattice introduces a varying electric potential across the length of the device, meaning that there is a varying probability of electrons occupying different positions over the length of the device. This one-dimensional multiple quantum well confinement leads to the splitting of the band of permitted energies into a number of discrete electronic subbands. See (b) in figure 2.1.

By suitable design of the layer thicknesses it is possible to engineer a population inversion between two subbands in the system which is required in order to achieve laser emission. Once an electron has undergone an intersubband transition and emitted a photon in one period of the superlattice, it can tunnel into the next period of the structure where another photon can be emitted. This process of a single electron causing the emission of multiple photons as it traverses through the QCL structure gives rise to the name *cascade*. Also it makes a quantum efficiency greater than usually possible which leads to higher output powers than semiconductor laser diodes.

Among the advantages of QCLs are the irrelevance of the Auger effect due to intersubband transitions and the achievement of emission at very long wavelengths, up to the THz region. It is also possible to tune the emission wavelength of QCLs

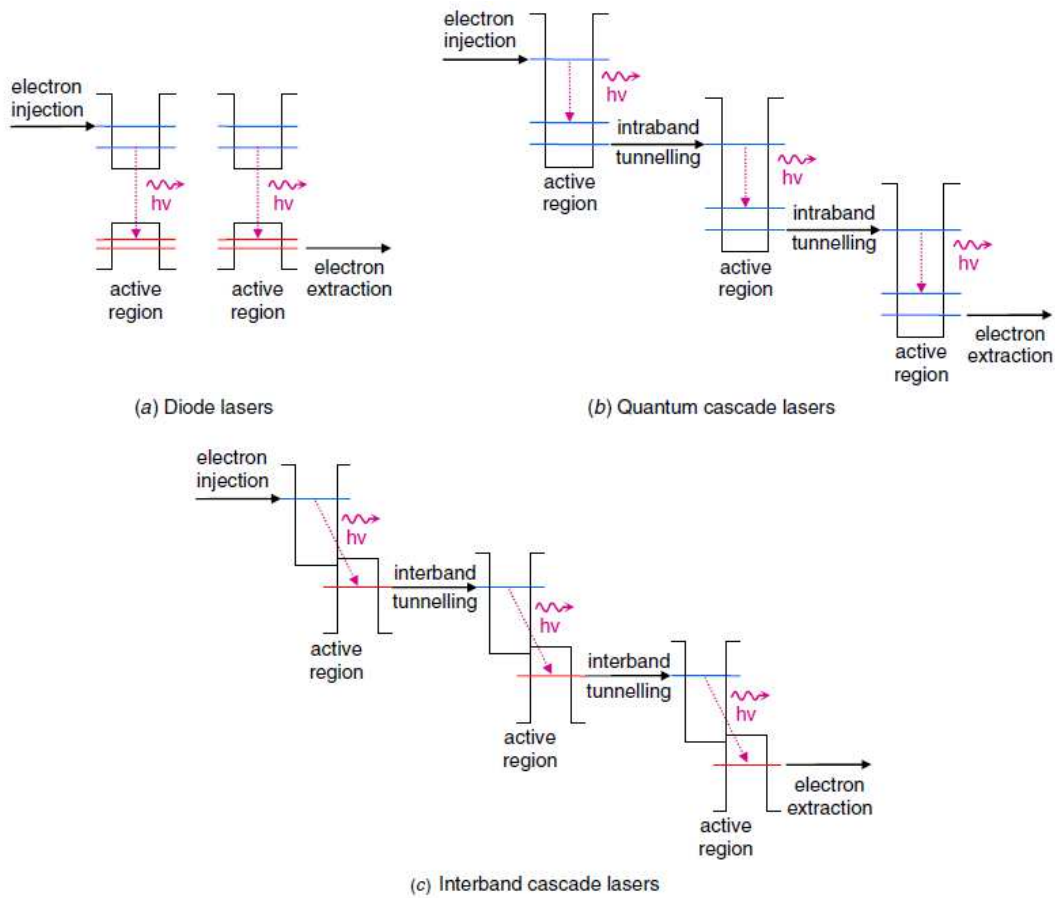


Figure 2.1: Comparison of the different transition processes for (a) diode lasers, (b) QCLs and (c) ICLs. Taken from [BRL<sup>+</sup>10]

over a wide range in the same material system [WFS<sup>+</sup>07, ZRC<sup>+</sup>09].

## 2.2 VECSEL Based on IV-VI Semiconductors

This work focuses on the Vertical External Cavity Surface Emitting Laser (VECSEL) based on IV-VI semiconductors. A very good beam quality over a large wavelength range in the Mid-IR has been achieved [Fil11] and the reasons for that will be explained in the following sub chapters.

### 2.2.1 IV-VI Semiconductors and their Properties

IV-VI materials have a direct narrow band gap of around 300 meV at room temperature. This, the low Auger coefficient and a very large band gap tunability are convenient features for Mid-IR lasers.

#### Crystal structure

As the name *lead salts* already indicates, IV-VI semiconductors like PbSe and PbTe crystallize in the face centered cubic structure like NaCl. By alloying  $\text{Pb}_{1-x}\text{Y}_x\text{Te}$  or  $\text{Pb}_{1-x}\text{Y}_x\text{Se}$  with  $Y=\text{Eu}, \text{Sr}$  or  $\text{Sn}$  the band gap is tuned by varying the composition  $x$  in the material.

The IV-VI materials are grown in layers by molecular beam epitaxy (MBE) on Silicon wafers. The lattice constant of the alloys  $\text{Pb}_{1-x}\text{Y}_x\text{Te}(\text{Se})$  is similar to each other but shows a large lattice mismatch with Silicon. A 2 nm thick layer of  $\text{CaF}_2$  is grown between the Si substrate and the IV-VI materials to overcome the lattice mismatch.

#### Band structure

IV-VI materials have a direct narrow band gap of around 300 meV at room temperature. At the four equivalent L-points of the Brillouin zone, the maxima of the valence band, respectively, minima of the conduction band are located and allow direct optical transitions. Conduction and valence bands are nearly mirror images of each other, resulting in almost identical effective masses for holes and electrons [NS83]. Figure 2.2 shows that the constant energy surfaces in k-space are four prolate spheroids (like cigars) orientated along the four equivalent [111] directions. The band gap of binary lead salts (PbTe, PbSe, PbS) can be thermally and chemically tuned over a wide range of the infrared spectrum. Unlike most other semiconductors, IV-VI materials exhibit a strong positive temperature dependence of the band gap of around 0.5 meV/K [Rav03], i.e. by increasing the temperature the cut-off wavelength decreases (see figure 2.3).

By alloying  $\text{Pb}_{1-x}\text{Y}_x\text{Te}(\text{Se})$  with  $Y=\text{Eu}, \text{Sr}$  or  $\text{Sn}$  the band gap is tuned by varying the composition ( $x$ ) in the material. For example PbTe can be alloyed with Sn (or SnTe with Pb) to set the band gap from 0.29 eV (PbTe) to 0.18 eV (SnTe). It

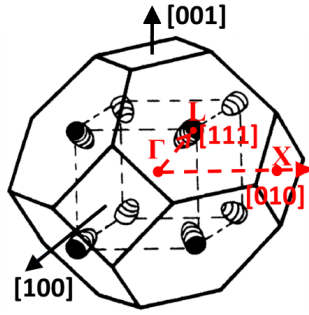


Figure 2.2: Brillouin zone of lead salts. The constant energy surface corresponds to four prolate spheroids orientated along the four equivalent  $[111]$  directions. Taken from [TACL71].

is important to note that the band gap in  $\text{Pb}_{1-x}\text{Sn}_x\text{Te}$  does not change linearly between the two extremes. The lead tin telluride alloys have narrower band gaps than their end point counterparts making lead tin telluride an ideal candidate for mid infrared applications [DMS66]. Therefore adding Sn to PbTe or PbSe decreases the band gap energy [TC67], while the addition of Eu [YKSB93] or Sr [PTC87] increases the band gap energy. Figure 2.4 shows empirical formulas for the calculation of lead salt band gaps.

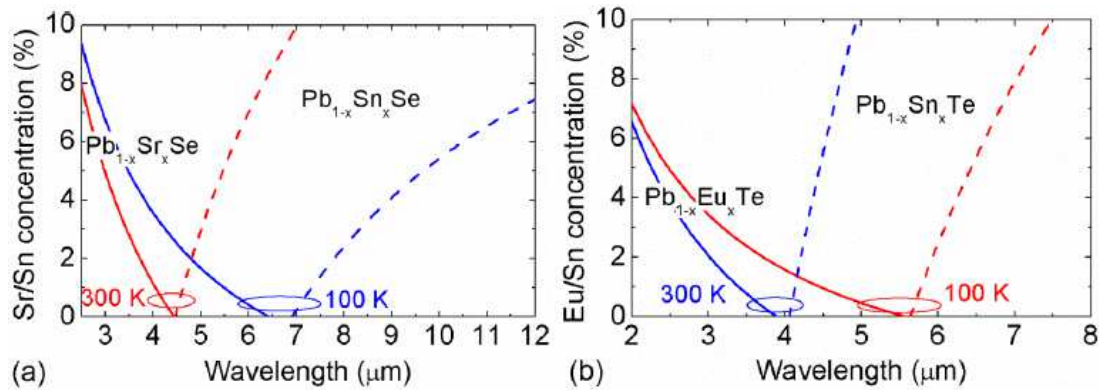


Figure 2.3: Band gap as a function of  $X$  ( $= \text{Sr}, \text{Eu}, \text{Sn}$ ) for  $\text{PbXSe}$  (a) and  $\text{PbXTe}$  (b) at 100 K and 300 K. Taken from [Khi14].

Material	Band gap [eV]
$\text{Pb}_{1-x}\text{Sr}_x\text{Se}$ ( $x < 27\%$ ):	$E_g(x, T) = 0.15 + 3.608x - 1.314x^2 + (0.43 - 3.093 + 6.495x^2) \cdot 10^{-3}T$
$\text{Pb}_{1-x}\text{Eu}_x\text{Se}$ ( $x < 5\%$ ):	$E_g(x, T) = 0.001 \cdot \left( 190 + \frac{0.51T^2}{T - 56} (1 - 9.8x) + 5880x \right)$
$\text{Pb}_{1-x}\text{Eu}_x\text{Te}$ ( $x < 5\%$ ):	$E_g(x, T) = 0.001 \cdot \left( 146.3 + \frac{0.475T^2}{T - 40.7} (1 - 3x) + 3000x \right)$
$\text{Pb}_{1-x}\text{Sn}_x\text{Te}$ ( $x < 20\%$ ):	$E_g(x, T) = 0.001 \cdot \left( 190 - 543x + \frac{0.045T^2}{T - 50} \right)$
$\text{Pb}_{1-x}\text{Sn}_x\text{Se}$ ( $x < 20\%$ ):	$E_g(x, T) = 0.001 \cdot \left( 125 - 1021x + \sqrt{400 + 0.256T^2} \right)$
$\text{Pb}_{1-x}\text{Se}_x\text{S}$ ( $0 < x < 100\%$ ):	$E_g(x, T) = 0.001 \cdot \left( 263 - 138x + \sqrt{400 + 0.265T^2} \right)$

Figure 2.4: Empirical formulas of the band gap as function of temperature and composition [And77, SYJ+02, YKSB93, PTC87, Pre79], Taken from [Khi14].

### Quantum Well (QW)

Quantum wells can be grown to further change the transition energy. Depending on the width of the wells and the band offsets between the conduction/valence band extrema of the barrier and well material a desired shift in transition energy (=design wavelength) can be realized.

QWs are defined as physical systems where carriers are confined along one dimension in one region of the space smaller than their characteristic de Broglie wavelength. Fabrication of QWs are made by embedding a sufficiently thin layer of a material with a lower band-gap (e.g. PbSe) into a semiconductor material with a higher one (e.g. PbSrSe). This way the semiconductor QW confines charge carriers in the dimension perpendicular to its surface, while in-plane movements within the layer are possible. In contrast to bulk material, the density of states changes from a square root to a step-like function (see figure 2.5). Therefore the density of states also becomes constant for the energy intervals between energetic eigenstates.

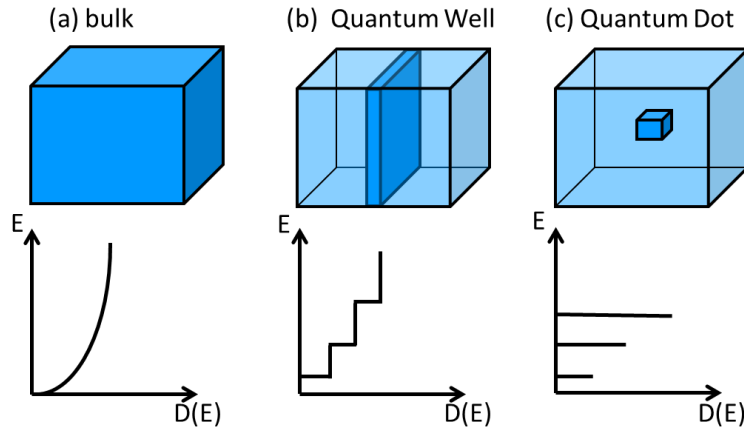


Figure 2.5: Charge carrier confinement and density of state: (a) bulk, (b) quantum well and (c) quantum dot [Khi14].

### Thermal properties

Thermal properties like the thermal conductivity are an important aspect for device applications. In our case of IV-VI compounds the thermal conductivity is comparatively low. While PbTe has a slightly higher thermal conductivity, different references show a range of 1.7 to 2.3 W/mK (at 300K) for PbSe and PbTe. Values for lead salt compounds like QWs are mostly unknown, but measurements of a multiple thin layer system of PbSe/PbSrSe and also for PbSe/PbSnSe show much lower thermal conductivity values compared to PbSe bulk material as reported in [Jef13]. Furthermore, they could show that the thermal conductivity decreases with thinner average layers in a superlattice system. Diffuse interface scattering of phonons is believed to be responsible for this effect. Lowering the cross-plane lattice thermal conductivity leads to a reduction of vertical heat flow through the layers and effects cooling of the sample, which is in contact with a heat sink. A possible solution for this problem regarding VECSEL devices could be a reduction in the number of layers as well as the growth of thicker layers. Also the magnitude of change for the thermal conductivity during lasing is unclear.

Another interesting property of lead salts is its very high dielectric constant with  $\epsilon > 150$  at RT and  $\epsilon > 10^3$  at low temperatures. The dielectric constant  $\epsilon$  can be expressed by the refractive index  $n$  and the extinction coefficient  $\kappa$  in

$$\epsilon = n^2 - \kappa^2 \quad (1)$$

which leads to high refractive indices for PbTe with  $n = 5.8$  and  $n = 5.0$  for PbSe at room temperature [YKSB93]. The refractive index changes with temperature and alloy composition, which can be combined with low refractive index materials to form a highly reflective Bragg mirror.

### The Auger recombination

The Auger recombination rate for lead chalcogenides is also well known for being very low. This process is a non-radiative recombination mechanism (see figure 2.6), where the energy created by an electron-hole-recombination is transferred to another electron (or hole), which is excited to a higher energy state in the band. Energy is conserved (instead of emitting the desired radiation) and the excited electron (or hole) relaxes down by releasing its energy in the form of lattice vibrations. In the Mid-IR, the Auger coefficient of bulk lead salts is around 100 times lower than of conventional III-V semiconductors.

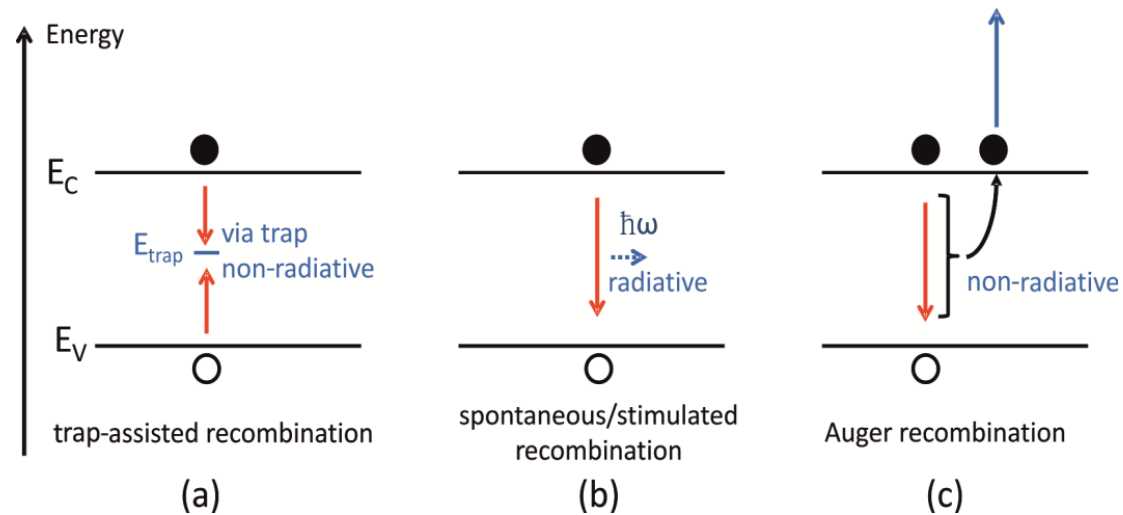


Figure 2.6: Schematic sketch of different recombination processes: (a) trap assisted recombination, (b) radiative recombination, (c) Auger recombination. Taken from [Khi14].

## 2.2.2 VECSEL Design

A Vertical-External-Cavity Surface-Emitting Laser (VECSEL) is a small semiconductor laser, where the laser light propagates perpendicular to the semiconductor wafer surface (surface-emitting). This is in contrast to conventional edge-emitting semiconductor lasers where the laser light propagates along the direction of the wafer surface and is usually emitted at a cleaved edge (edge-emitting).

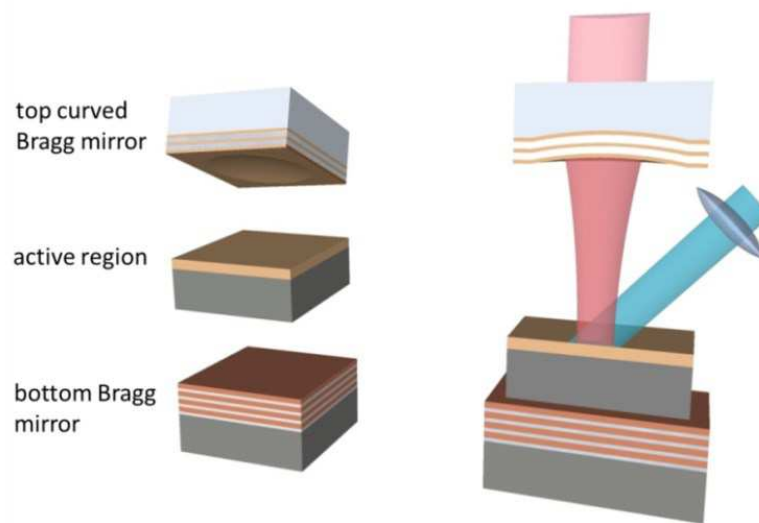


Figure 2.7: Schematic sketch of the modular VECSEL design. The active region and bottom Bragg mirror are fabricated on to separate substrates. The bottom chip is realized by putting both parts together without any bonding material.

Another major difference to edge-emitters is the relatively short interaction length of the laser beam with the optical active material (often several QWs) of less than 100 nm, compared to several 100  $\mu\text{m}$  up to 2 mm or longer. The optical gain is therefore only in the region of a few percent and it is essential to minimize the losses in the cavity by using Bragg mirrors with a high reflectivity. Unlike a VCSEL, in which two high-reflective Distributed Bragg Reflectors (DBRs) are incorporated into the semiconductor structure to form the optical cavity, in a VECSEL one of these mirrors (in our case the top one, see figure 2.7) is placed outside (*External*) the semiconductor structure and forms an external cavity. The optically pumped gain region is typically very thin compared to the lateral dimensions of the beam

and this significantly also minimizes the effect of "antiguinding" non-linearities in the diode laser gain region. The result is a large-cross-section single-mode optical beam which is not attainable from edge-emitting diode lasers.

By changing the length of the external cavity, for example by applying a voltage on the Piezoelectric driver on the top mirror, the VECSEL becomes a continuous wavelength tunable single mode laser. See figure 2.8.

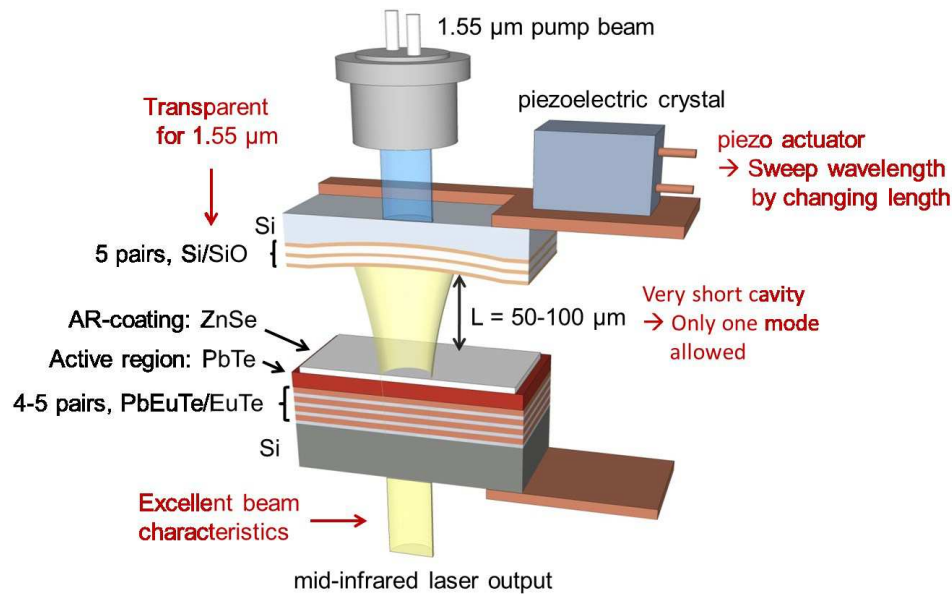


Figure 2.8: Schematic illustration of a continuously tunable single mode VECSEL. The laser light couples out through the bottom mirror. The top mirror is mounted on piezo-actuator enabling to change continuously the cavity length. Taken from [Khi14].

The VECSEL can be used in reflection mode (see figure 2.7), where the laser light couples out through the top mirror, or in transmission mode (see figure 2.8), where the laser light couples through the bottom mirror. The reflection mode is more likely to be used although it is more difficult to align due to the need of a precise incident angle. Still, the VECSEL has the advantage of not having to be radiation penetrable.

## 2.3 Gas Detection

Absorption spectra in each spectral regions have different cause of characteristics, as shown in figure 2.9.

Spectral region	Cause of absorption
UV (200–400 nm)	Electronic transitions
Near IR (700 nm–2.5 $\mu\text{m}$ )	Molecular vibration and rotation, first harmonic
Mid IR (2.5–14 $\mu\text{m}$ )	Molecular vibration and rotation, fundamental

Figure 2.9: Cause of absorption in different regions of the electromagnetic spectrum

In the so-called fingerprint region of the infrared, gas phase absorption spectra exhibit narrow lines as a result of molecular vibrations at discrete energy levels. These can be measured at high resolution, resolving the line, or at lower resolution, measuring the absorption band.

Optical gas detection using absorption spectroscopy is based on application of the Beer–Lambert Law [JIC88];

$$I = I_0 \exp(-\alpha l) \quad (2)$$

where  $I$  is the light transmitted through the gas cell,  $I_0$  is the light incident on the gas cell,  $\alpha$  is the absorption coefficient of the sample (typically with units of  $\text{cm}^{-1}$ ) and  $l$  is the cell's optical path length (typically with units of cm). By comparing the absorption coefficients of pure gas components with the measured absorption coefficient of the sample, the desired concentrations of the components within the sample can be determined.

Additionally, the wavelength tuning allows to scan with a narrow line width across individual gas absorption lines at very high resolution. This is an advantageous feature for many spectroscopic applications.

### 3 Measurement

The first step to create an optionally upgradeable and accurate simulation model in the new *COMSOL Multiphysics*<sup>®</sup> version is based on the simplest form of chip that can be measured as an operating laser in a Photoluminescence spectroscopy (PL). For this project PbSe bulk chips without any mirrors were chosen. See c) in figure 3.1.

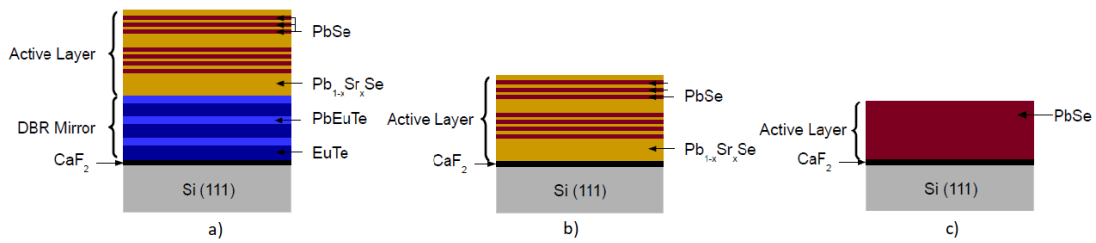


Figure 3.1: Complexity levels of VECSEL chips: a) QW chip with Bottom DBR mirror (it normally has a top mirror as well, see 2.7), b) QW chip without mirrors and c) Bulk chip without mirrors. The Si layer thickness is strongly reduced in these sketches.

#### 3.1 Experimental Setup

Figure 3.2 shows a sketch of the measurement setup. The excitation laser is mounted on a XYZ-stage to enable correct alignment of the focus point in both modes. In transmission mode the excitation laser beam goes into the vacuum cryostat chamber and hits the surface of the chip as shown in figure 3.3. For reflection mode the excitation laser beam goes into the vacuum cryostat chamber to first hit a gold mirror and be reflected on the surface of the chip as shown in figure 3.3 from the other side.

The holder is mounted on a cold finger which is cooled down by a liquid nitrogen tank that can be refilled from the outside. The temperature of the cold finger and holder is stabilized by a proportional–integral–derivative (PID) controller and a heating resistor.

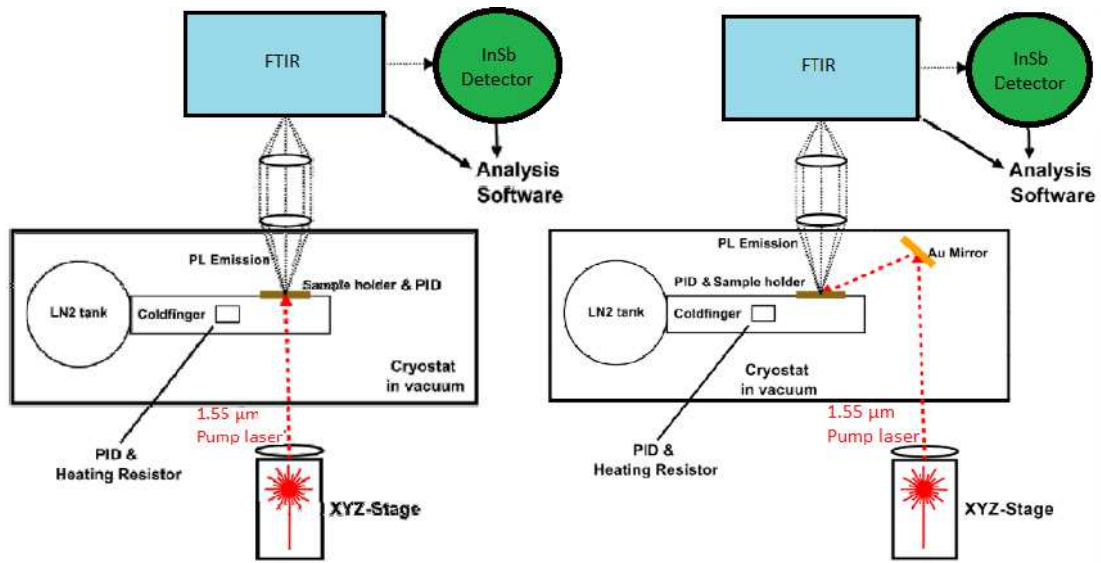


Figure 3.2: Sketch of the PL measurement setup in transmission mode (left) and in reflection mode (right)

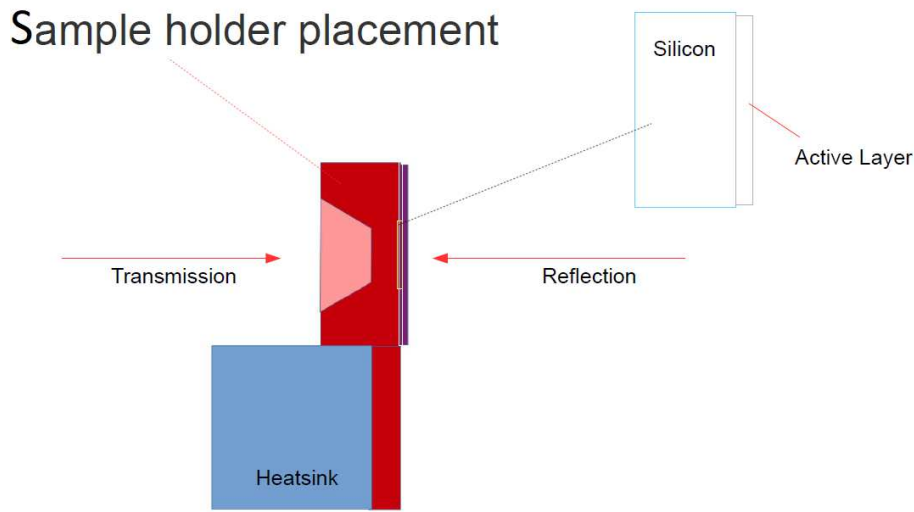


Figure 3.3: Sketch of the chip holder of the PL measurement setup with the incident excitation laser beam in transmission mode (left) and in reflection mode (right).

The emitted PL emission of the chip exits the chamber from the front side and is collected by a collimating lens which directs the signal towards the focusing lens,

where it is directed into the entrance window of the Fourier-transform infrared spectroscopy (FTIR). The FTIR disperses the signal before it reaches the InSb thermal image detector where the beam intensity is measured and then the spectrum can be registered in the FTIRs software program OPUS.

Measurement setup settings like *mode* (transmission mode or reflection mode), *T\_heatsink* (temperature of heatsink), *pump\_vol* (voltage of pump laser, therefore laser power), *z\_f* (distance from focus point) and *f\_l* (focal length of lens) already impact the results strongly, which is why they are implemented as parameters into the *COMSOL Multiphysics*<sup>®</sup> simulation model. All the parameters are presented in figure 4.11.

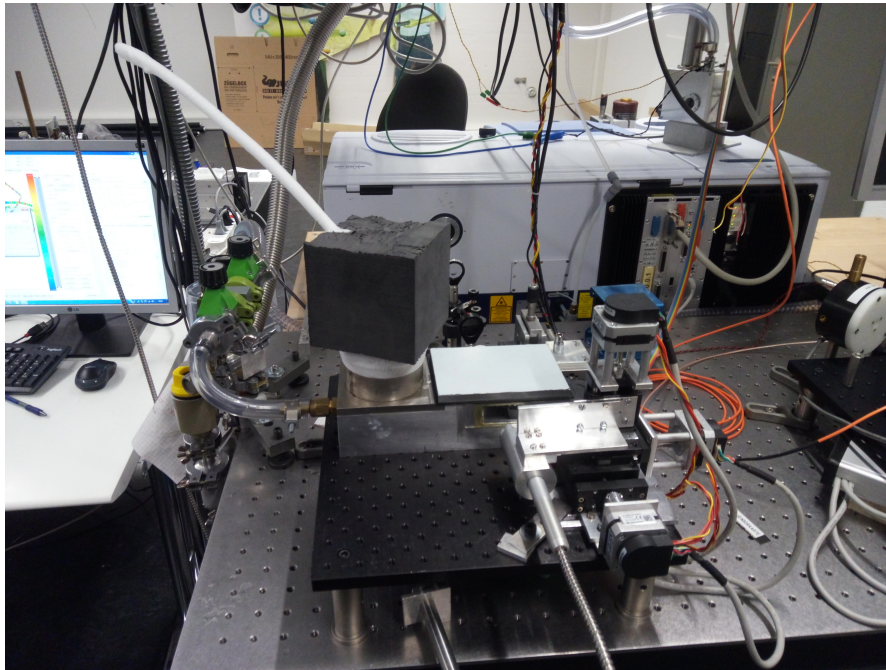


Figure 3.4: Photo of the actual measurement setup.

## 3.2 Post Processing

The FTIRs software program OPUS can be set to do the background noise correction, which is why we always also have to measure once with the pump laser turned off, the 0V spectrum. Since carbon dioxide has two vibrational bands in the IR spectrum, this has to be corrected by a linear function in our post processing

scripts. There, the detection response function of the InSb thermal image detector is also considered.

### 3.3 Measurement Results

#### 3.3.1 Special Measurements

Several different kinds of measurements have been done on this setup to understand the physics and to implement the right parameters into the *COMSOL Multiphysics*<sup>®</sup> simulation model.

After the delicate work of inserting and aligning the laser chip in two space axes into the setup, the third axis has to be aligned with the distance from excitation laser to the chip. This is done by finding the focus point of the pump laser's Gaussian beam stepwise as shown in figure 3.5.

The focus point is indicated by the maximum wavenumber and the lowest spectra integral since the high energy density in focus leads to high chip temperature and inefficient photoluminescence.

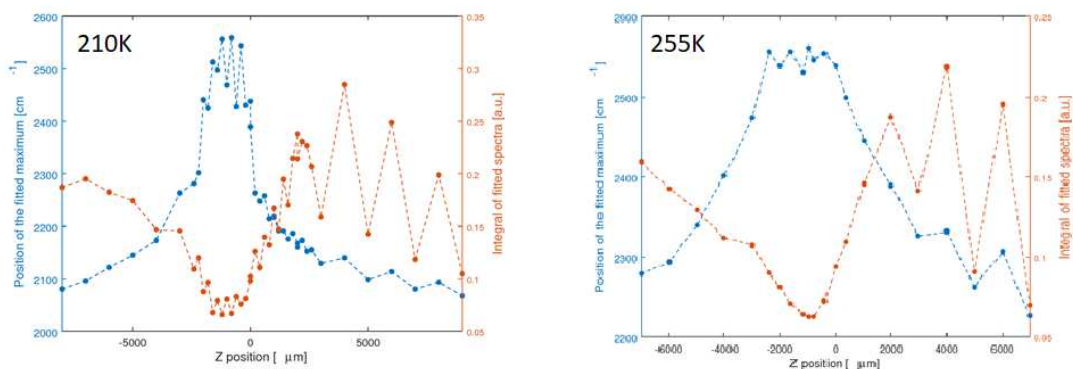


Figure 3.5: These two graphs show the stepwise approach of finding the focus point at two different heatsink temperature by marking the maximum wavenumber and the integral of spectra for every z position.

Another measurement was to understand the effect of the Germanium filter at different positions, see figure 3.6. It is used to block the pump laser wavelength from entering the InSb thermal image detector but also absorbs other wavelengths partly.

Therefore the Germanium filter and detector should be positioned with awareness of its absorption effects.

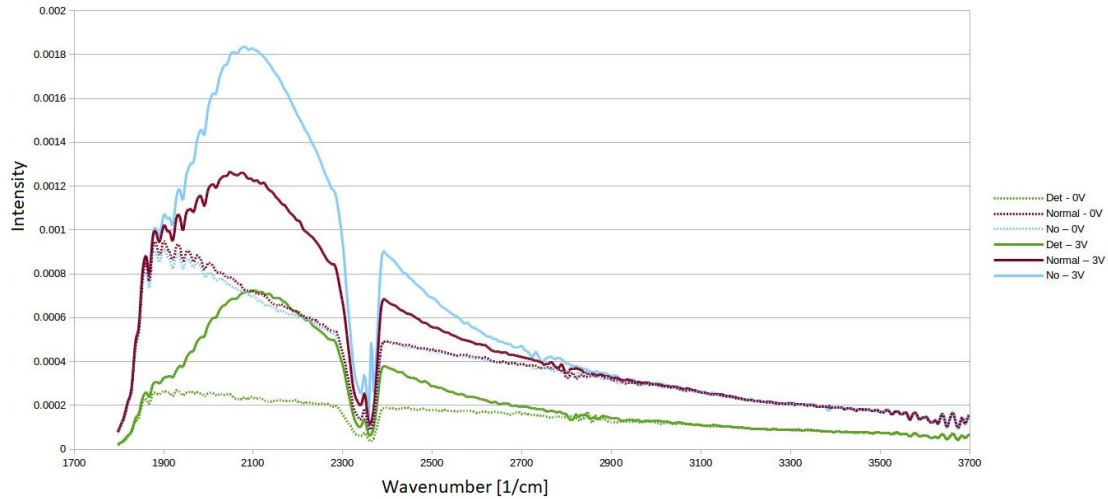


Figure 3.6: Comparison of intensity measurements for three different positions ('Det' = right before the InSb thermal image detector, 'Normal' = after the cryostat and before the FTIR, 'No' = Germanium filter is not used) with a pump laser set to 3V and without the use of pump laser 0V.

The absorption coefficient of PbSe bulk chips is one of the most important parameters for the *COMSOL Multiphysics*<sup>®</sup> simulation model. Literature has different numbers for it and therefore it had to be checked in our measurement setup as well. For that, the pump laser hits the chips on both surfaces and for each the reflection and transmission is measured with a power meter.

Measured Absorption coef. for 1832	Measured Absorption coef. for 1787	Measured Absorption coef. for 1738	Simulation Absorption coef. <sup>1</sup>	Other literature absorption coef. <sup>2</sup>
$3.39 \pm 0.5$ (15%)	$3.72 \pm 0.36$ (9.6%)	$3.46 \pm 0.28$ (8.1%)	3.86	3.6

Figure 3.7: Measurement results of the three PbSe Bulk chips with different thicknesses of the active region at room temperature (chip #1832 with  $0.7 \mu\text{m}$ , chip #1787 with  $1.2 \mu\text{m}$  and chip #1738 with  $1.7 \mu\text{m}$ ) with the old simulation absorption coefficient. <sup>1</sup>...[YKSB93] and another literature value <sup>2</sup>...[SSA95] in units of  $[\mu\text{m}^{-1}]$

Measuring error grows with lower thickness due to inaccuracy of it and the effects of refraction through the layers (see figure 3.1c). The resulting absorption coefficient for PbSe in our *COMSOL Multiphysics*<sup>®</sup> simulation model should therefore simulate the value  $\alpha = 3.53 \mu\text{m}^{-1}$ .

For the absorption coefficient we calculate

$$\alpha = \frac{4\pi\kappa(T, E)}{\lambda} \quad (3)$$

with  $\kappa$  based on the extinction coefficient function from [YSP02] and the above mentioned correction based on our measurements in figure 3.7. The wavelength  $\lambda = 1.55 \mu\text{m}$  is of the laser light from our pump laser.

### 3.3.2 Photoluminescence Spectroscopy (PL) Results

The three chips, differing in thickness, #1832 with  $0.7 \mu\text{m}$ , #1787 with  $1.2 \mu\text{m}$  and #1738 with  $1.7 \mu\text{m}$  of PbSe as the active layer were measured at least at four different heat sink temperatures, four different focus lengths and six different pump laser voltages (with 0V for background noise correction) in reflection mode. A complete measurement of a chip includes up to twelve different heat sink temperatures. The most used spectra for the simulation model of these chips are shown in figure 3.8. The following effects are the results of the spectra interpretation.

Emission-based effects:

- Higher Sr-content moves band-gap to higher wavenumbers. This is known by comparing to measurements of PbSrSe Bulk chips and is confirmed by literature [SYJ+02].

Thermal effects:

- Lower distance to focus point broadens the curve and increases the wavenumber of the peak.
- Higher thickness of active layer moves band-gap to higher wavenumbers, stronger effect with Reflection mode.
- Higher laser pump voltage moves band-gap to higher wavenumbers and increases intensity of curve.

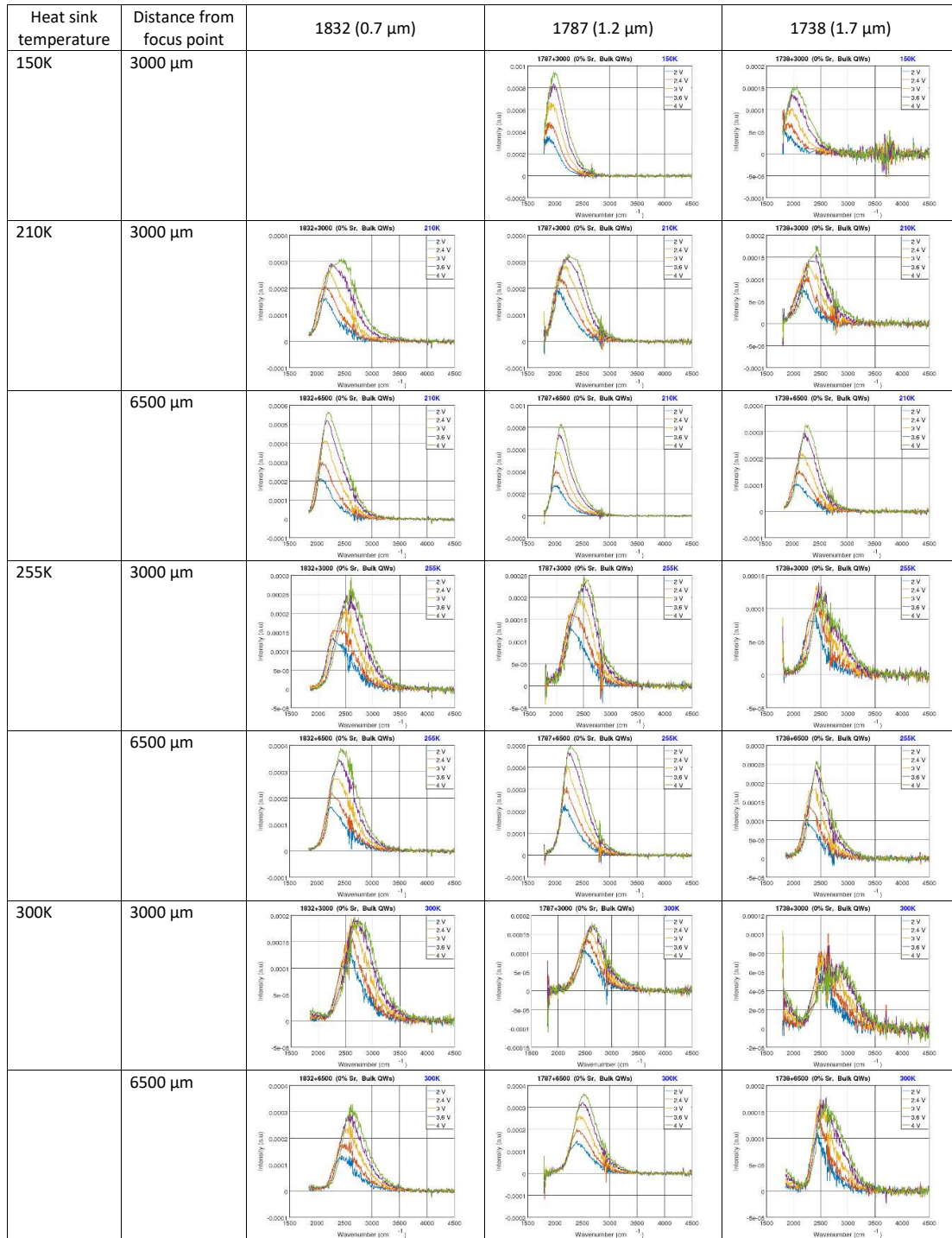


Figure 3.8: Table of several measured spectra from the chips #1832 with 0.7  $\mu\text{m}$ , #1787 with 1.2  $\mu\text{m}$  and #1738 with 1.7  $\mu\text{m}$  PbSe Bulk active layer at heat sink temperatures 150K, 210K, 255K and 300K with distances from the focus point of 3 mm and 6.5 mm. The used voltages of the pump laser were 2, 2.4, 3, 3.6 and 4V.

## 4 Simulation: Heat profile in COMSOL Multiphysics®

COMSOL Multiphysics® explains its product [com]:

COMSOL Multiphysics® is a general-purpose simulation software for modelling designs, devices, and processes in all fields of engineering, manufacturing, and scientific research. The platform product can be used on its own or expanded with functionality from any combination of add-on modules for simulating electromagnetism, structural mechanics, acoustics, fluid flow, heat transfer, and chemical engineering.

We used the platform product in combination with the *Heat Transfer module*.

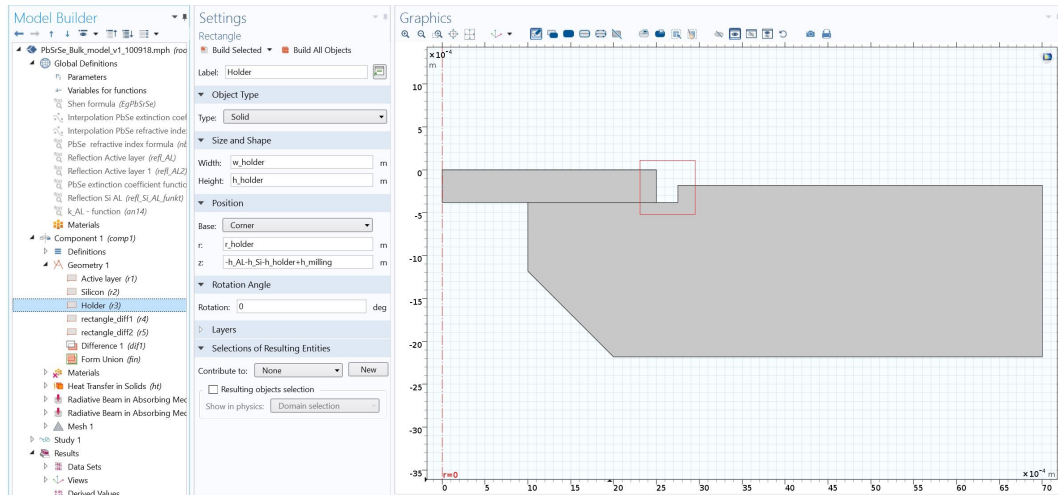


Figure 4.1: The 2D cross sectional area in COMSOL Multiphysics® with a very thin layer on top as the active layer followed by the thicker block of Silicon. These two layers build the chip in this model and is put on the biggest part, the aluminium holder. The red marked rectangle is zoomed in on in figure 4.2.

Firstly, the geometry of the chip and holder is designed as a parametrized geometry to easily change the sizes of the model at any time. It is drawn in 2D as a cross sectional area (like figure 3.1 with the holder) and is then automatically rotated into an axisymmetric 3D model. This round geometry is a good approximation of the

real cuboid shape and uses the rotational symmetry for more efficient simulation calculation.

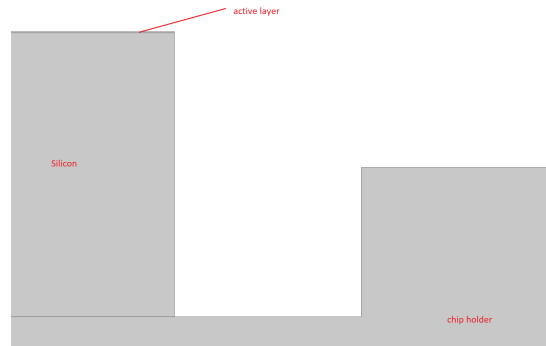


Figure 4.2: Enlarged picture of the red marked rectangle in figure 4.1 shows part of the very thin active layer.

Then the materials for each geometry section were chosen from the material library or in case of PbSe the material properties had to be manually configured. This also included the right absorption coefficient (see section 3.3.1) and thermal conductivity. The *Radiative Beam in Absorbing Media* interface from the *Heat Transfer Module* is used to model the attenuation of the pump laser light going through the chip, and the heat generated by the absorption. The effect of the Gaussian beam propagation (see figure 4.3) is also taken into account by giving the distance from the focus point to the chip as the parameter  $z_f$  and the focus length of the used lens as the parameter  $f_l$  in. The Gaussian beam parameters in figure 4.3 all rely on  $z_f$ ,  $f_l$  and the pump laser properties. Their values and relations can be seen in figure 4.11.

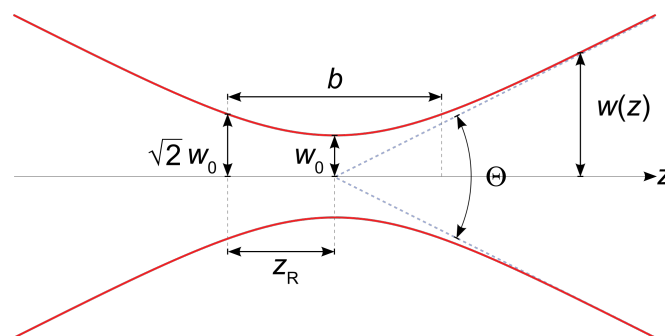


Figure 4.3: The Gaussian beam shape as a function of several parameters from figure 4.11

The different beam orientation and incident intensity for transmission or reflection mode is set by an if-function depending on the set mode in the parameters. This is also thought-out for every reflection at the boundaries of all layers; vacuum, active layer and Silicon. Depending on the operating mode (reflection or transmission) the pump laser light has to travel through different layers until it reaches the active layer.

If the active layer is thin enough and did not absorb the total pump laser light, part of the rest pump laser light will propagate into the next layer, while the other part of the rest pump laser light which reflected at the layer transition will be absorbed again through the active layer. The difference in intensity values (the color scales maxima are varying!) between the thicker chip in figure 4.4 & 4.5 and the thinner chip in the figure 4.6 & 4.7 makes this effect clear.

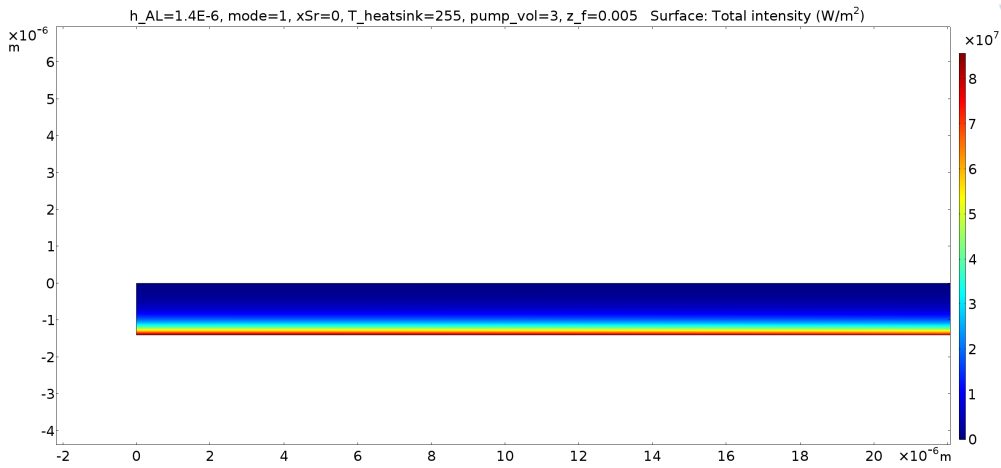


Figure 4.4: Incident beam in transmission mode: Radiation intensity [ $\text{W}/\text{m}^2$ ] vs area [ $\text{m}^2$ ] plot of a simulation with a  $1.4\ \mu\text{m}$  PbSe-bulk chip showing a zoomed in part of the active layer center in *COMSOL Multiphysics*<sup>®</sup> simulation model.

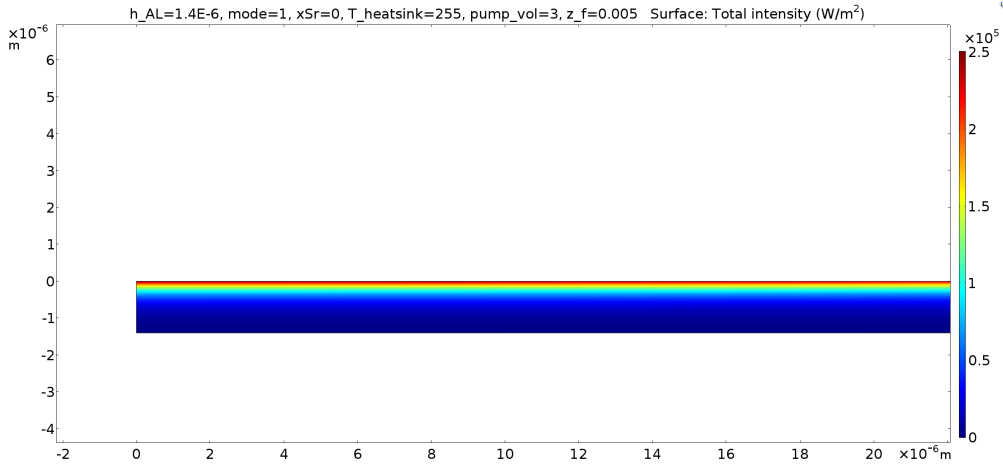


Figure 4.5: Back reflected beam in transmission mode: Radiation intensity [W/m<sup>2</sup>] vs area [m<sup>2</sup>] plot of a simulation with a 1.4  $\mu\text{m}$  PbSe-bulk chip showing a zoomed in part of the active layer center in *COMSOL Multiphysics*<sup>®</sup> simulation model.

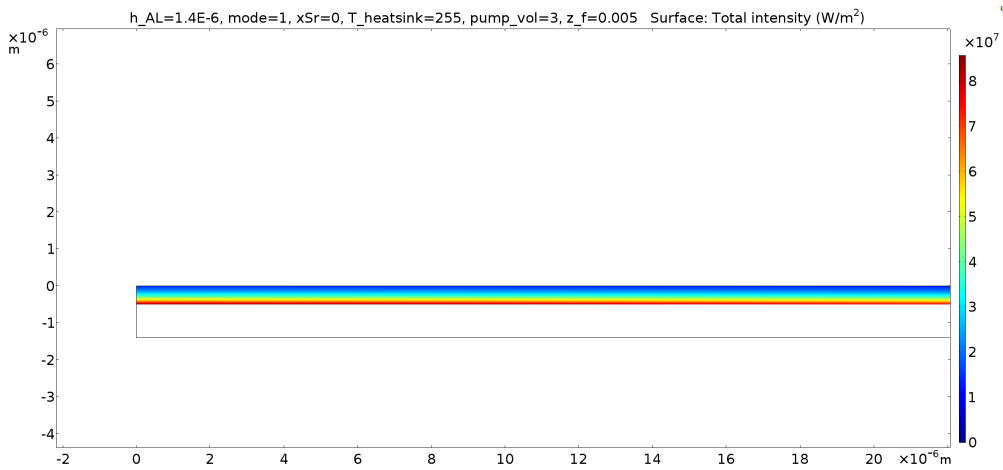


Figure 4.6: Incident beam in transmission mode: Radiation intensity [W/m<sup>2</sup>] vs area [m<sup>2</sup>] plot of a simulation with a 0.5  $\mu\text{m}$  PbSe-bulk chip showing a zoomed in part of the active layer center in *COMSOL Multiphysics*<sup>®</sup> simulation model.

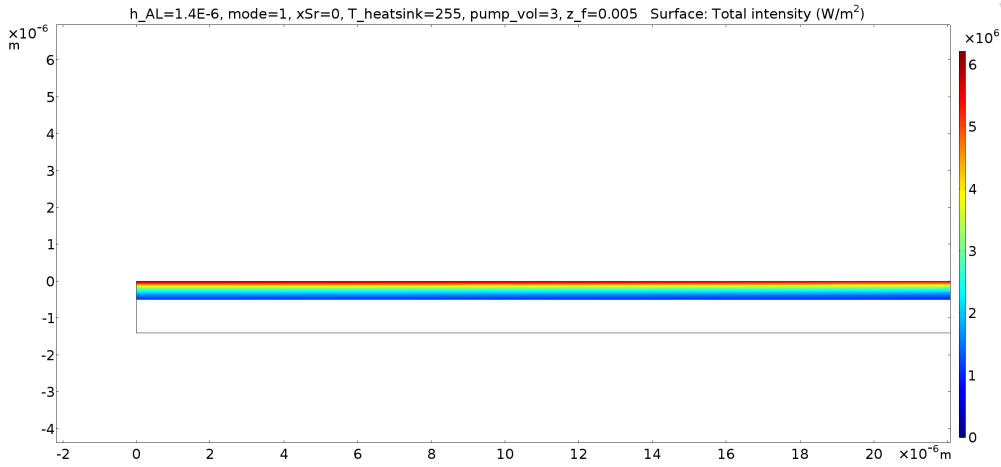


Figure 4.7: Back reflected beam in transmission mode: Radiation intensity [W/m<sup>2</sup>] vs area [m<sup>2</sup>] plot of a simulation with a 0.5 μm PbSe-bulk chip showing a zoomed in part of the active layer center in *COMSOL Multiphysics*<sup>®</sup> simulation model.

The reflectance calculation for every layer transition is done with the refractive index and extinction coefficient of every involved material.

To calculate the reflectivity we assume normal incidence of the pump laser light through the interface of layer 1 and layer 2

$$R = \frac{(n_1 - n_2)^2}{(n_1 + n_2)^2} \quad (4)$$

with the complex refractive index

$$n = n' - i\kappa \quad (5)$$

$n'$  is the real part of the refractive index, while the imaginary part  $\kappa$  is called extinction coefficient.

As already mentioned in section 3.3.1, in case of the PbSe active layer, a refractive index function and an extinction coefficient function with temperature and band gap energy dependence are used [YSP02] with a correction based on our measurements in figure 3.7.

After introducing the *Radiative Beam in Absorbing Media* with all the extra features to simulate laser light behaviour and its absorption for both modes, the next step

is to simulate the after effects of the mentioned energy absorption. This energy absorption causes heat generation and needs to be transferred through the whole setup to the heat sink. For that the *Heat Transfer in Solids* module will be used for the whole setup. It models the stationary solution for heat fluxes through all the components and therefore the heat profile of the setup. The input properties are the thermal conductivity, density and heat capacity at constant pressures of every material. Several boundaries and the heat source have to be defined as well. Since the whole setup is in a vacuum cryostat (see figure 3.2) there is no heat convection with ambient air and most boundaries have to act as thermal insulation. Figure 4.8 shows the thermal insulation of our model.

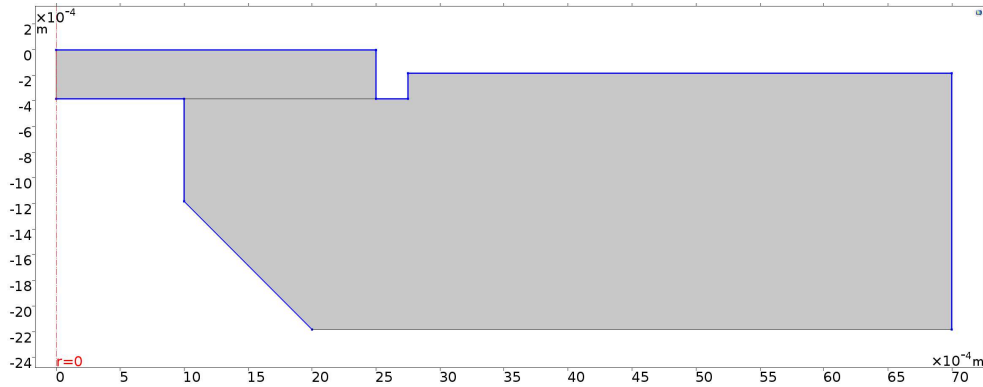


Figure 4.8: The blue edges are set as insulating boundaries in the *COMSOL Multiphysics*<sup>®</sup> simulation model, since they can not exchange heat with vacuum.

Only two edge lines are not blue in figure 4.8 because the upper left is the center axis for the 3D axisymmetric 3D model and the bottom right, because that is where the chip holder is connected to the heatsink. Correspondingly, that boundary has been set to have the constant heatsink temperature (see figure 4.9), which can be set in the parameters (like figures 4.11 and 6.1).

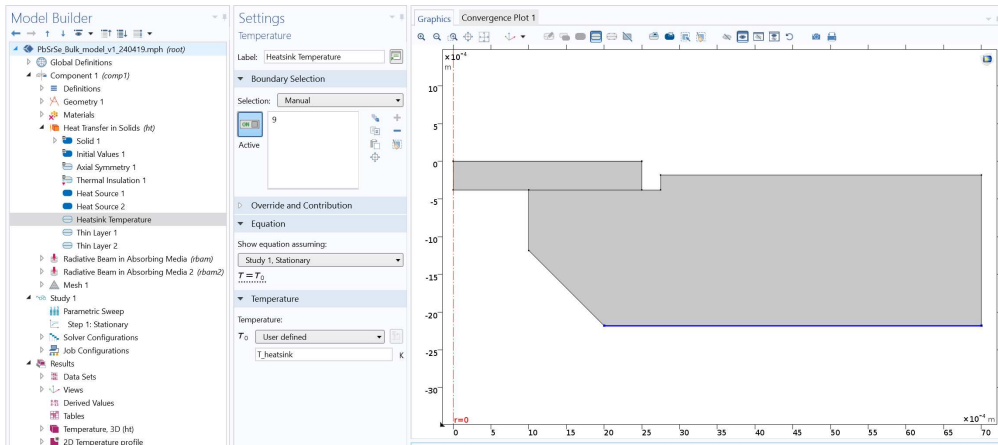


Figure 4.9: The blue edge is the boundary for the heat sink temperature in *COMSOL Multiphysics*<sup>®</sup> simulation model.

The last step for the *Heat Transfer in Solids* module is to set the heat source itself. In our case it is a radiation heat source from the pump beam and we defined the laser radiation twice as heat source for the active layer; once for the incident beam and once for the back reflected beam.

COMSOL also uses the finite element method (FEM), which is a numerical method for solving problems of engineering and mathematical physics. It includes the use of mesh generation techniques for dividing a complex problem into small elements. The complex problem is usually a physical system with the underlying physics as in our case the heat equation expressed in either partial differential equations (PDE) or integral equations, while the divided small elements of the complex problem represent different areas in the physical system. Our model has very differently sized components and also areas with varying interest for us, which make it necessary to manually set each mesh.

A very dense mesh for the center of the active layer was chosen, since most radiation absorption is happening there. To save computational time, the mesh density decreases with distance from the center of the chip. It also has been set in way that the mesh density is independent of the chip thickness to have comparable simulation quality for every chip. See the results in figure 4.10.

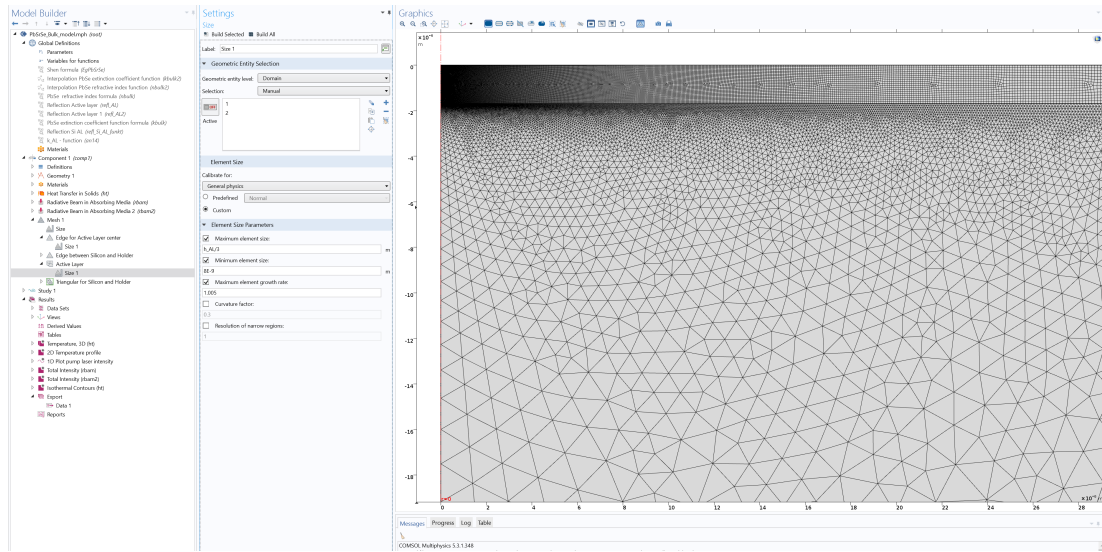


Figure 4.10: Visible meshgrid of the chips center showing that the mesh density decreases with distance from the center to save computational time in *COMSOL Multiphysics*<sup>®</sup> simulation model.

Name	Expression	Value	Description
mode	-1	-1	"1" for Transmission, "-1" for Reflection
h_AL	1.693E-6[m]	1.693E-6 m	height of active layer
xSr	0	0	Strontium content in PbSrSe-Bulk
k_AL	if(mode== -1,if(Intensity_pump<7,0.09*Intensity_pump+(exp(h_AL/1)/um...)	2.4641 W/(m·K)	thermal conductivity function of active layer for Reflection mode, Transmission mode is constant 2.2
T_heatsink	300[K]	300 K	temperature of heatsink
pump_vol	4	4	Voltage of pump laser
z_f	5e-3[m]	0.005 m	distance from focus point
f_l	125e-3[m]	0.125 m	focus length of lens
w_AL	2.5e-3[m]	0.0025 m	width of active layer
h_Si	380e-6[m]	3.8E-4 m	height of silicon
w_Si	2.5e-3[m]	0.0025 m	width of silicon
h_holder	2e-3[m]	0.002 m	height of holder
w_holder	6e-3[m]	0.006 m	width of holder
r_holder	1e-3[m]	0.001 m	corner position of holder (radius of holder hole), if set to "0" the holder hole disappears
pump_wl	1.55e-6[m]	1.55E-6 m	wavelength of the pump laser
w_L	0.002475[m]	0.002475 m	collimated CW laser beam radius
M_square	1.07	1.07	M <sup>2</sup> of CW laser
w_0	pump_wl*M_square*sqrt(pi)/(pi*w_L)	2.6662E-5 m	gaussian beam radius at focus
w_0_lit	26.5e-6[m]	2.65E-5 m	for comparison only
z_r	w_0^2*pi/(M_square*pump_wl)	0.0013466 m	Rayleigh range
w_z	w_0*(1+(z_f/z_r)^2)^0.5	1.0253E-4 m	gaussian beam radius with distance z_f from focus point
sigma	w_z*0.5	5.1264E-5 m	standard deviation for (rbam)
sigma_old	0.5*w_0_lit*(1+(z_f/z_r)^2)^0.5	5.0951E-5 m	for comparison only
refl_au_mirror	0.985	0.985	Reflectivity of gold mirror in Reflection mode
trans_cryo_front_window	0.95	0.95	Transmissivity of cryostat front glass window
w_z_b	w_0*(1+(z_f+h_AL/z_r)^2)^0.5	1.0256E-4 m	gaussian beam radius with distance z_f from focus point height of active layer for back reflection of beam
sigma_b	w_z_b*0.5	5.128E-5 m	standard deviation for (rbam2) for back reflection of beam
k_i_Si_holder	0.1[W/(m·K)]	0.1 W/(m·K)	thermal conductivity of interface between Si and holder
h_i_Si_holder	10.0e-6[m]	1E-5 m	height of interface between Si and holder
roh_i_Si_holder	2730 [kg/(m^3)]	2730 kg/m <sup>3</sup>	density of interface between Si and holder (Aluminium)
cp_i_Si_holder	893 J/(kg·K)	893 J/(kg·K)	heat capacity of interface between Si and holder (Aluminium)
h_milling	200e-6[m]	2E-4 m	height of milling from holder
abs_fac	0.91	0.91	Absorption factor for correction
Intensity_pump	(0.865*(1.07267*pump_vol-1.00851)[W]/(w_z^2*pi))[m^2/W]*10E-8	8.597	Intensity of pump laser on chip surface for calculation of k_AL
Intensity_pump_real	(0.865*(1.07267*pump_vol-1.00851)[W]/(w_z^2*pi))	8.597E7 W/m <sup>2</sup>	real Intensity of pump laser on chip surface
CaF2_k	0.024	0.024	

Figure 4.11: Parameters in the *COMSOL Multiphysics*<sup>®</sup> simulation model.

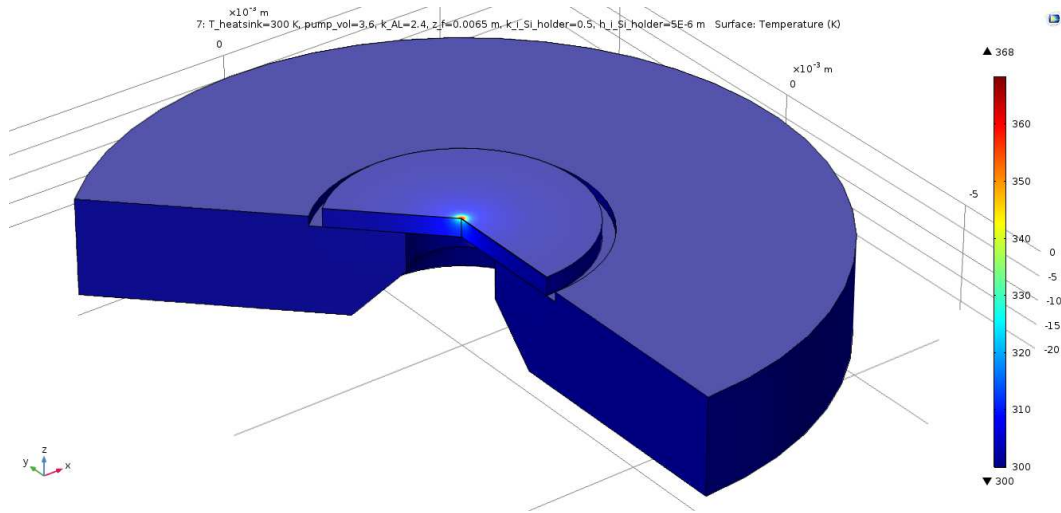


Figure 4.12: The 3D simulation result shows the calculated temperatures in Kelvin by a colour scale.

COMSOL reveals the temperature due to absorption but more importantly, it provides us the amount of power that is absorbed from the pump beam in every volume element. These solutions can be visualized in various plots (will be shown in the section 6.3) in COMSOL and helps to understand the underlying physics. The next step is to simulate an emission spectrum based on the solution data of COMSOL.

## 5 Simulation: Emission spectrum in Octave

The script converts COMSOLs solution into an emission spectrum. Afterwards it plots a comparison of the simulation results with the measurements.

It is programmed in **GNU Octave**, which is a software featuring a high-level programming language, primarily intended for numerical computations and is mostly compatible with MATLAB. It is a free software under the terms of the GNU General Public License.

The first part of the script is *user input*, where the same parameters as in COMSOL should be set. Then the script reads in the data sets from the saved COMSOL solutions as a temperature profile ( $r, z, T, P$ ) with the geometric coordinates  $r$  and  $z$ , the temperatures  $T$  and the absorbed energy  $P$  for each volume element of the active layer. This can be done for several solutions at once to be able to compare several spectra in one plot. The Sr contents have to be set as well, since the band gap energy calculations depend on them (see formula in figure 2.4).

The second part reads in the experimental data from the measurements. The simulated and measured data sets are saved in different forms and are also handled very differently throughout the script:

- The COMSOL data is exported as .TXT-files with the four columns ( $r, z, T, P$ ). This data needs to be converted into an emission spectrum via temperature distribution & broadening effects, which will be explained in the following subsections.
- The measurement data is saved as .DPT-files. They are registered emission spectra (wavenumber vs. intensity) from the InSb thermal image detector and the FTIRs software program OPUS. These measurements needs to be corrected for the detector efficiency (a signal calibration for each wavenumber) and the background noise (subtraction of the measured emission with turned off pump laser, the 0 V spectrum). The  $CO_2$  absorption hole is also replaced with a linear approximation between the wavenumbers  $2250\text{ cm}^{-1}$  and  $2400\text{ cm}^{-1}$ .

They are brought into a comparable form for the final plot of this script.

More input parameters and physical constants can then be defined.  $T_0$  for the

temperature dependent luminescence function has also been set (see formula (11) and its effect in figure 5.4).

## 5.1 Temperature distribution

The goal is to convert the temperature and energy profile of the active layer into an emission spectrum. To do so we use the first formula in figure 2.4, which we call Shens band gap formula, named after the first author of its publication [SYJ<sup>+</sup>02]. We use it to match COMSOLs calculated temperatures to band gap energies for every volume element of the active layer with dependence of the chips Sr content. These band gap energy values can then be converted to wavenumbers, which is necessary for the aimed emission spectrum.

To get a wavenumber relative intensity the volume elements with equal temperatures have to be summed up to understand how many volume elements contribute to the same temperature and therefore to an emission of the same wavenumber. This results in a volume histogram in figure 5.1, which shows that most of the volume elements contribute to the temperature near 300 K, which was the heatsink temperature for this simulation. The indicated becomes more clearly visible in figure 4.12 where the vast volume of the chip is colored as dark blue.

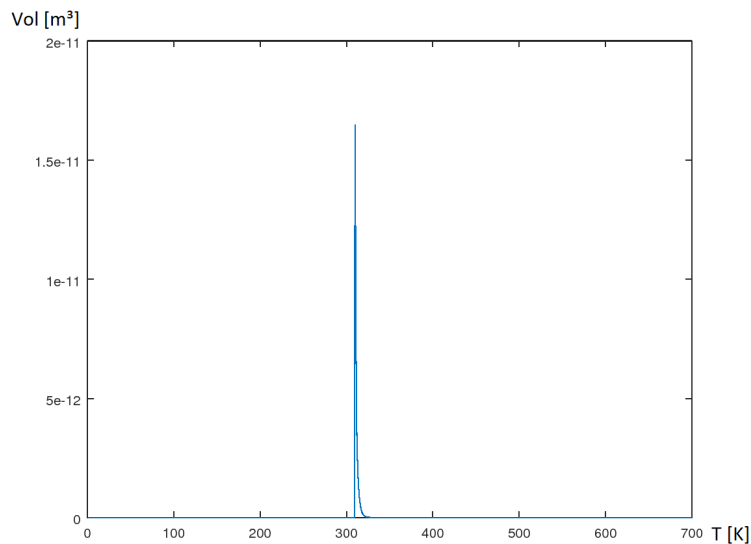


Figure 5.1: Volume-Temperature distribution in the active layer.

With the right distribution in place, we now have to take into account how much energy has been absorbed to reach these temperatures. We let COMSOL calculate and export these values (see figure 5.2) by

Expression	Unit	Description
T	K	Temperature
(rbam.Itot+rbam2.Itot)	W/m <sup>2</sup>	Radiation intensity of incident beam and back reflected beam
(rbam.Itot+rbam2.Itot)*meshvol	W	Radiation power
(rbam.Itot+rbam2.Itot)*meshvol*rbam.kappaR	W/m	Absorbed power per penetrated length
(rbam.Itot+rbam2.Itot)*meshvol*rbam.kappaR*r*2*pi	W	Total absorbed power

Figure 5.2: COMSOL expression for the variable export calculation for the total absorbed power for every mesh volume element. Only the first and last line matters, the rest is for dimension control.

with

$$rbam.Itot \text{ [W/m}^2\text{]} \dots \text{ Radiation intensity of incident beam} \quad (6)$$

$$rbam.Itot2 \text{ [W/m}^2\text{]} \dots \text{ Radiation intensity of back reflected beam} \quad (7)$$

$$meshvol \text{ [m}^2\text{]} \dots \text{ mesh volume element, surface dimension due 2D modeling} \quad (8)$$

$$rbam.kappaR \text{ [m}^{-1}\text{]} \dots \text{ absorption coefficient of PbSe} \quad (9)$$

$$2 * r * \pi \text{ [m]} \dots \text{ circumference circle to get the volume element} \quad (10)$$

We then match these power values to the volume histogram for every temperature and get the Power-Temperature distribution in figure 5.3.

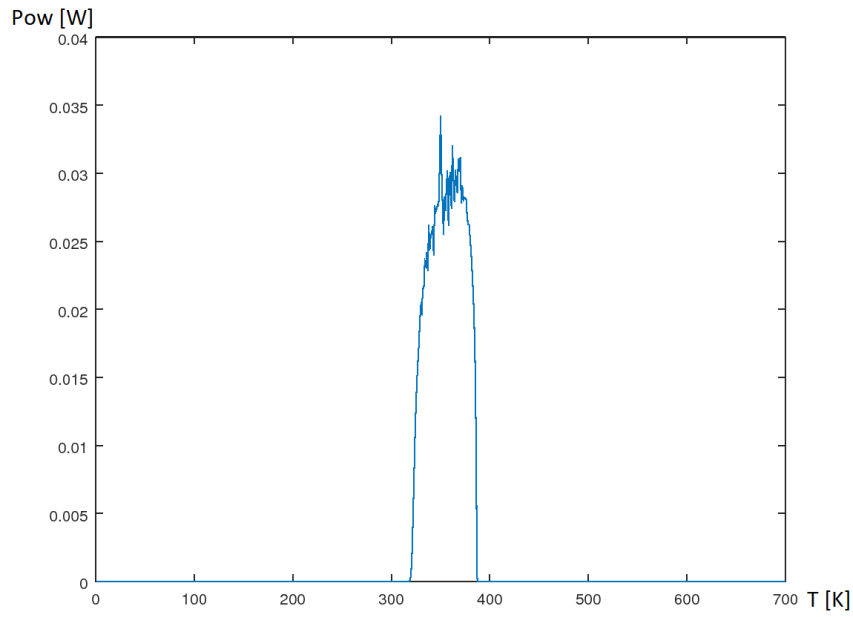


Figure 5.3: Power-Temperature distribution in the active layer.

The next step is to also take into account that with higher energies the loss in the process of converting absorbed light from the pump laser into an emission will also increase. The here used temperature dependent luminescence function is a rough approximation just for our model [PV12]

$$f(x) = \frac{1}{1 + \exp(\frac{T}{T_0})} \quad (11)$$

is multiplied with the absorbed power from figure 5.3 and results to the distribution in figure 5.4.

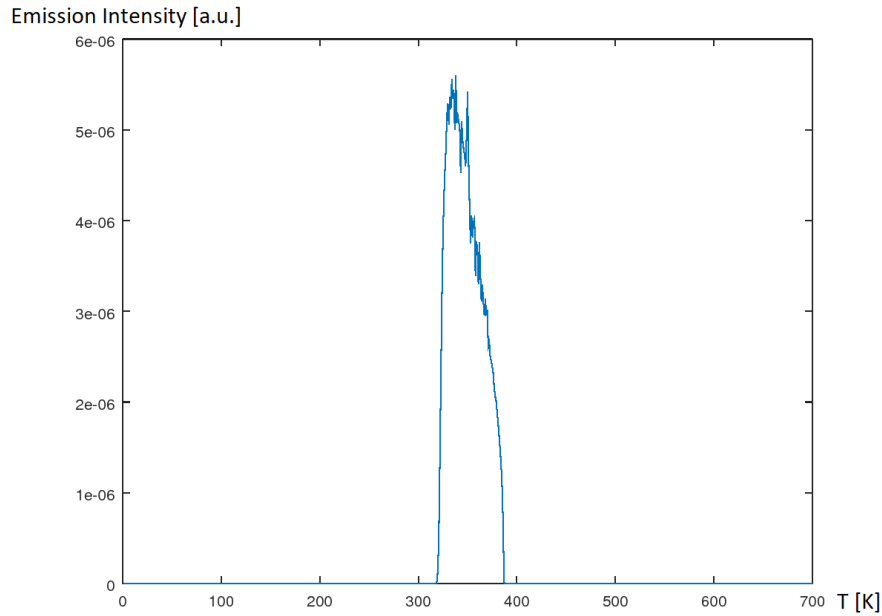


Figure 5.4: Emission Intensity (Absorbed Power with loss due temperature dependent luminescence)-Temperature distribution in the active layer.

For the explanation the x-axes of the figures showed the corresponding temperature values. At any time Shens band gap formula can be used to match COMSOLs calculated temperatures to band gap energies. These band gap energy values can then be converted to wavenumber, which will show the sought after emission-wavenumber spectra.

For more details, especially for PbSe/PbSrSe quantum wells, Shen et al. explained and measured spectroscopic line shape broadening mechanisms in [SJWW02].

## 5.2 Broadening effect

The above achieved intensity values are built on the assumption that the intensities belong exactly to their corresponding wavenumber's band gap energy. This is not true, since the density of states at the exact band gap energy is zero. That is the reason why the temperatures have not been converted to band gap energies yet as mentioned above. Therefore the temperature dependent occupation probability and density of states have to be considered as well. My preceding student included this

with the Fermi–Dirac distribution for the spontaneous- and stimulated emission.  
The implementation in the Octave script:

for  $i=1:\text{length}(\text{TempList})$

$$\begin{aligned}
 & \text{intensity\_T\_Fermi}_{(i:\text{end})} = \text{intensity\_T\_Fermi}_{(i:\text{end})} \\
 & + \frac{\text{intensity\_T}_i \cdot \sqrt{\hbar \cdot c \cdot k\_shen_{(i:\text{end})} - \hbar \cdot c \cdot k\_shen_i}}{\exp\left(\frac{100 \cdot (\hbar \cdot c \cdot k\_shen_{(i:\text{end})} - \frac{\hbar \cdot c \cdot k\_shen_i}{2})}{k_B \cdot \text{TempList}_i}\right) + 1} \\
 & + \frac{\text{intensity\_T}_i \cdot \sqrt{\hbar \cdot c \cdot k\_shen_{(i:\text{end})} - \hbar \cdot c \cdot k\_shen_i}}{(\exp\left(\frac{100 \cdot (\hbar \cdot c \cdot k\_shen_{(i:\text{end})} - \frac{\hbar \cdot c \cdot k\_shen_i}{2})}{k_B \cdot \text{TempList}_i}\right) + 1)^2}
 \end{aligned} \tag{12}$$

endfor

with

$$\text{TempList} \dots \text{temperature array of all available temperatures} \tag{13}$$

$$\text{intensity\_T\_Fermi}_{(i:\text{end})} \dots \text{Fermi-Dirac distributed intensity array} \tag{14}$$

from current  $i$  to the last temperature

$$\text{intensity\_T} \dots \text{undistributed intensity from figure 5.4} \tag{15}$$

$$k\_shen \dots \text{wavenumber converted with Shens band gap formula} \tag{16}$$

$$\text{the factor } 100 \dots \text{is due the wavenumber conversion from } \text{cm}^{-1} \text{ to SI} \tag{17}$$

That broadens the curve massively and now the already mentioned conversion from temperatures to band gap energies can be done. This is also the last calculation step in the Octave script, followed only by data and plot handling.

# 6 Usage - How to Simulate and Compare in COMSOL and Octave

## 6.1 Introduction

The COMSOL Bulk model and Octave script allow the simulation of an emission profile for a PbSrSe Bulk chip. Firstly, the necessary parameters need to be set in the user input in COMSOL to simulate a temperature profile ( $r$ ,  $z$ ,  $T$ ,  $P$ ) with the geometric coordinates  $r$  and  $z$ , the temperatures  $T$  and the absorbed energy  $P$  for each volume element of the active layer.

Then the Octave scripts converts this profile to an emission spectrum and adds temperature distribution & broadening effects. Afterwards a comparison of simulation results and measurements is possible.

## 6.2 Parameters for user input and computing in COMSOL

In case the general measurement set-up stays unchanged, only these parameters under Parametric Sweep node need to be adjusted in the *Parameter value list* (see figure 6.1) input depending on the:

- chosen chip (height of active layer, Strontium content and thermal conductivity of active layer),
- laser settings (Voltage of pump laser) and
- set-up settings (Transmission- or Reflection-mode, temperature of heatsink and distance from focus point).

The *Parametric Sweep* must be enabled by right-clicking on it (highlighted *Disable/Enable*). Many different values (each value is separated by a comma) can be set for all possible parameters. Parameters can be added, sorted and deleted in the red box. A thought-out order of parameters makes the following data export and use easier.

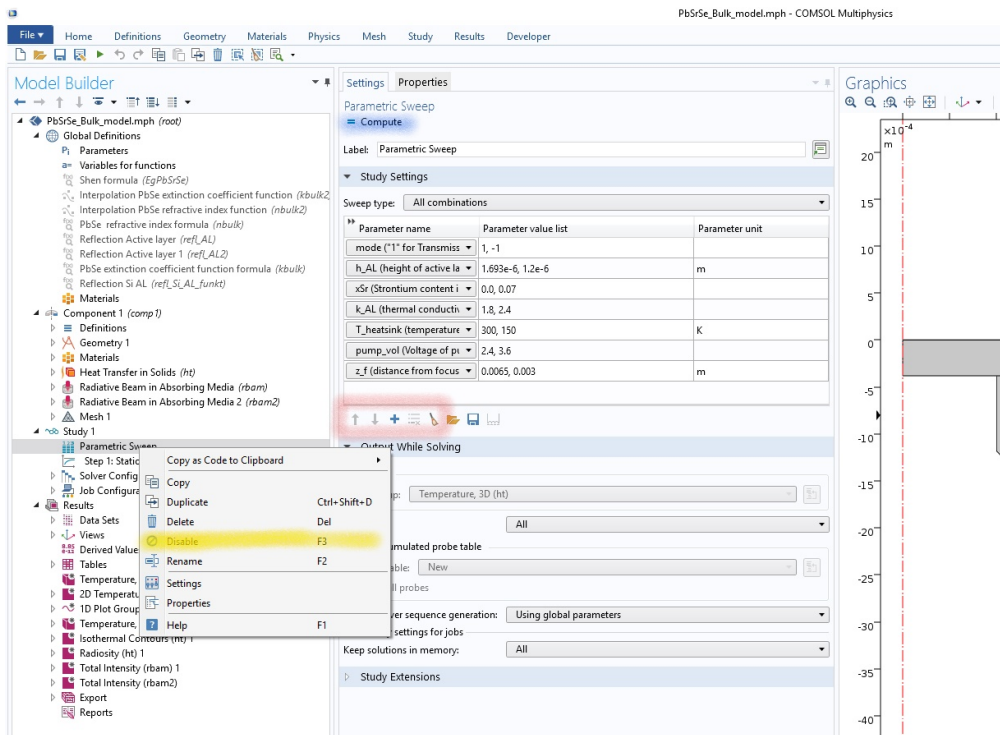


Figure 6.1: *Parameter value list* in the *COMSOL Multiphysics*<sup>®</sup> simulation model.

After the parameters and its values have been chosen, the computation can be started by clicking on **Compute**. COMSOL will now solve the model for every parameter combination.

### 6.3 Plots & data export in COMSOL and emission spectrum in Octave

After the computation is done, the results can be studied in COMSOL by the different plot nodes (e.g. “Temperature, 3D (ht)”, “2D Temperature profile”, “Total Intensity (rbam)”, ...) under *Results*. There the solution and its parameter values can be chosen and plotted. Under *Data Sets* the selection of the Parametric Solution has to be set to *domain 2* (=active layer), see figure 6.2. For the 2D plots select the same *Parametric Solution* (see figure 6.3), while for 3D plots *Revolution 2D* has to be selected (see figure 6.4). Following figures show the different plotting possibilities of the *COMSOL Multiphysics*<sup>®</sup> simulation model results.

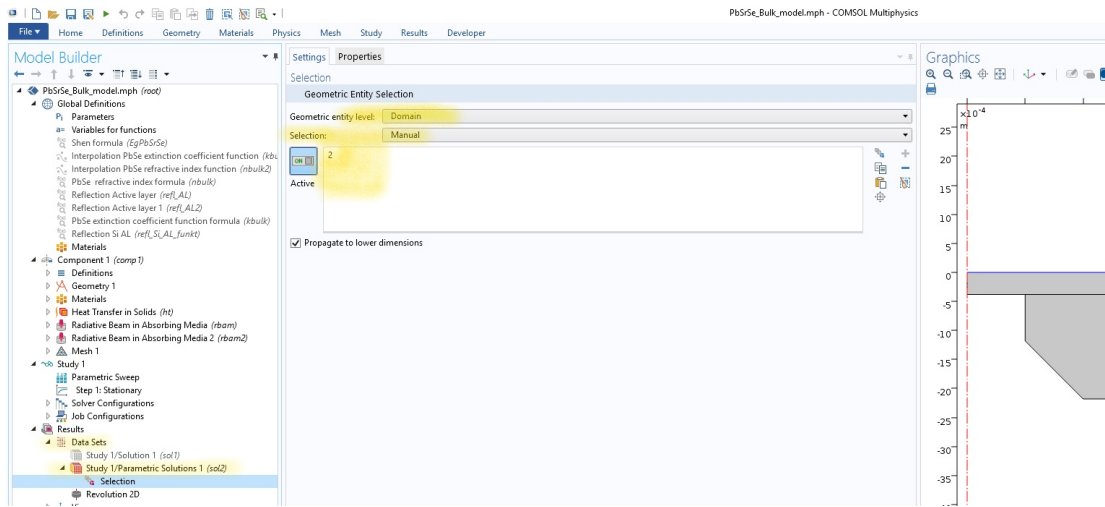


Figure 6.2: Data set selection for the active layer in the *COMSOL Multiphysics*<sup>®</sup> simulation model. Notice that domains, entire geometry, boundaries or points can be selected for the data export and plots.

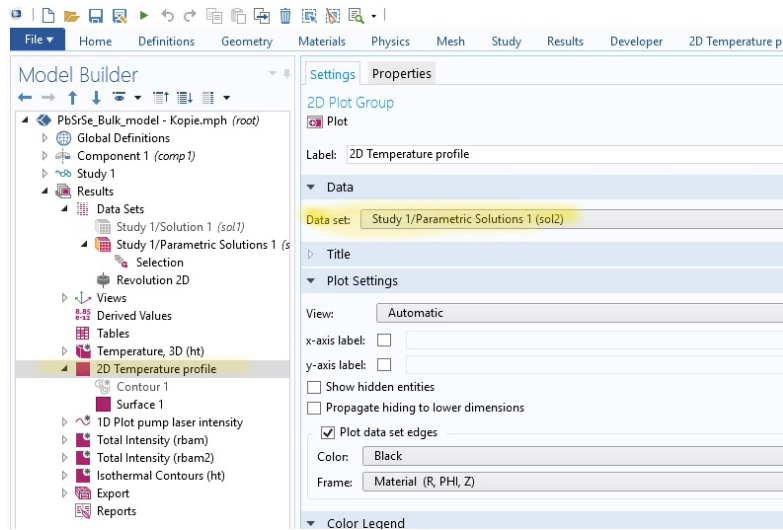


Figure 6.3: 2D plots data set selection in the *COMSOL Multiphysics*<sup>®</sup> simulation model.

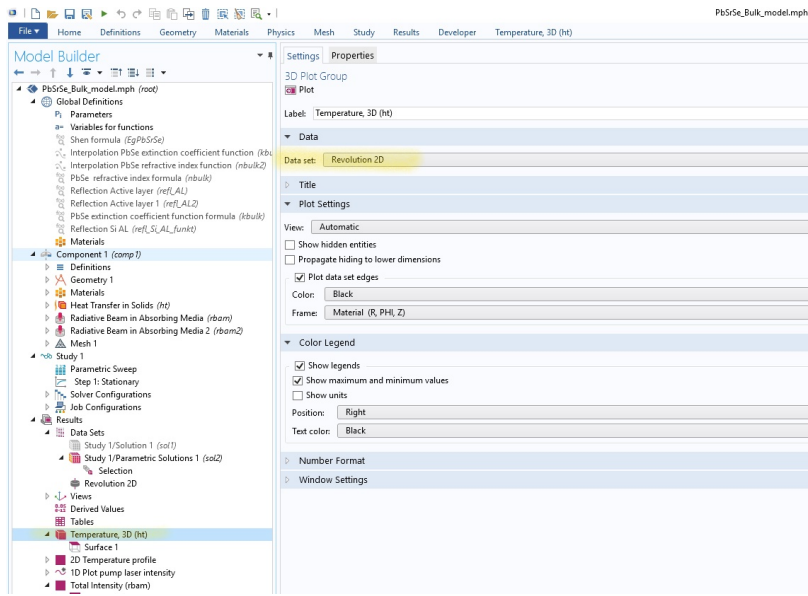


Figure 6.4: 3D plots data set selection in *COMSOL Multiphysics*<sup>®</sup> simulation model.

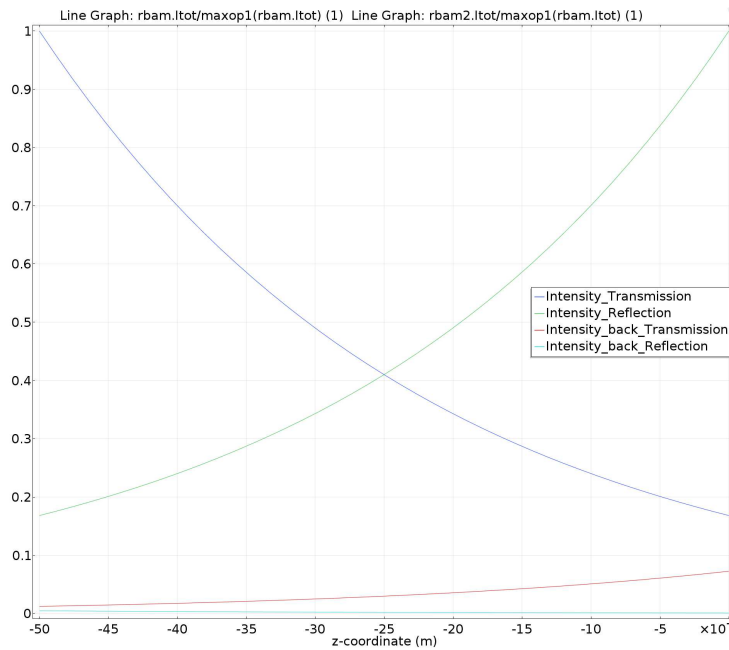


Figure 6.5: A 1D line graph plot in *COMSOL Multiphysics*<sup>®</sup> simulation model: Another way of visualizing the radiation intensity from the figures 4.6 & 4.7 is to graph all their normalized values together. The beam reflected back in reflection mode is weaker because of lower reflection at the interface active layer-silicon than at the interface active layer-vacuum.

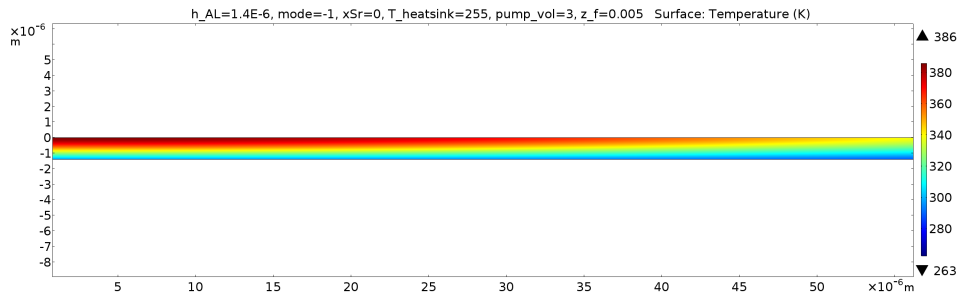


Figure 6.6: A 2D temperature profile in *COMSOL Multiphysics*<sup>®</sup> simulation model: The same simulation result and similar to the figures 4.4 & 4.5 the cross section temperature profile can be visualized.

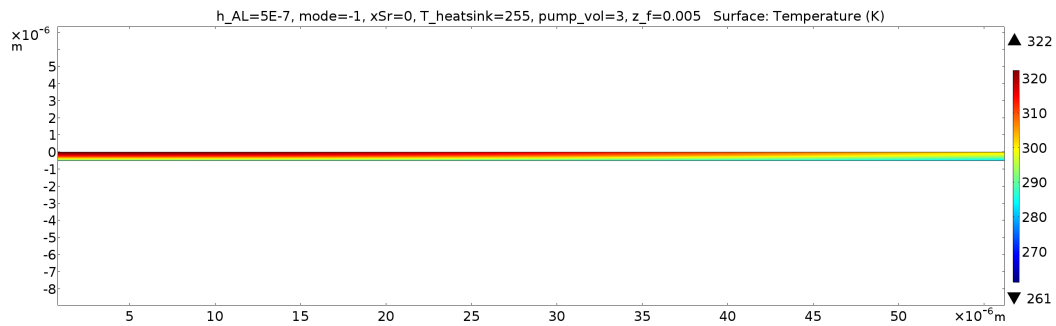


Figure 6.7: A 2D temperature profile in *COMSOL Multiphysics*<sup>®</sup> simulation model: The same simulation result and similar to the figures 4.6 & 4.7 the cross section temperature profile can be visualized. Notice the lower maximum temperature due the thinner active layer.

Figure 4.12 shows the whole 3D model with a temperature colour scale.

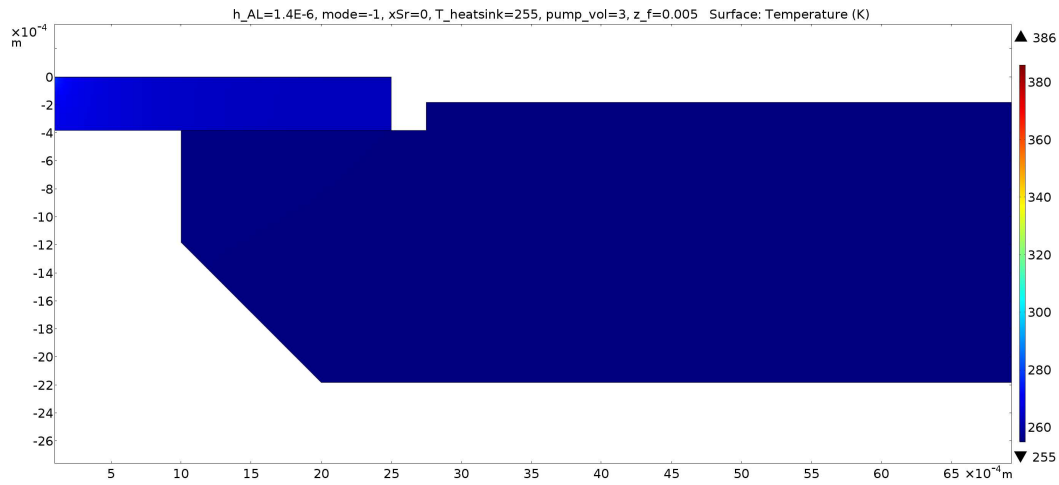


Figure 6.8: A 2D temperature profile in *COMSOL Multiphysics*<sup>®</sup> simulation model of the whole holder.

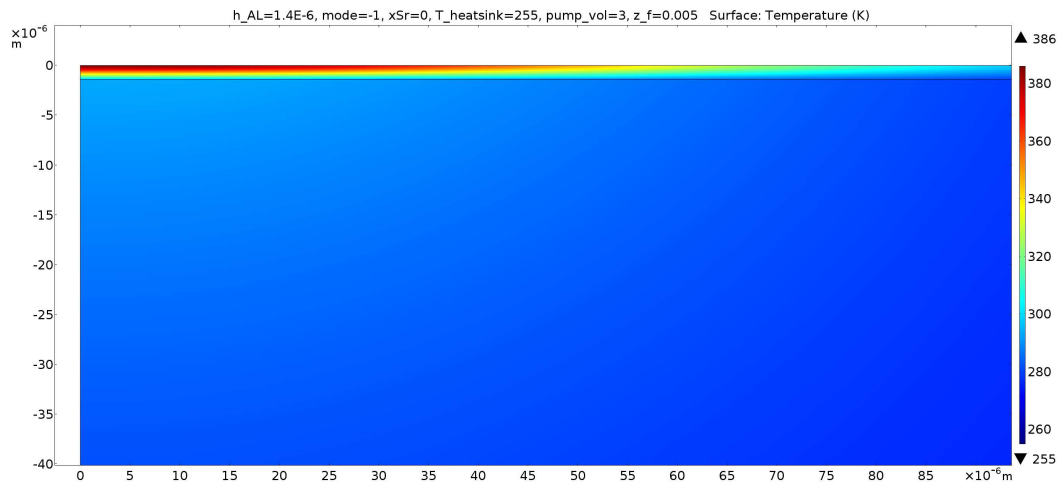


Figure 6.9: A 2D temperature profile in *COMSOL Multiphysics*<sup>®</sup> simulation model zoomed in to the active layer of the previous figure 6.8.

The results can be exported under the *Export* node. With a parametric sweep each parameter set can be individually chosen (highlighted Parameter selection options and with the *Ctrl* key more than one Parameter value can be chosen). Every selection can then be exported into a .TXT-file by clicking on the red marked *Export* button as shown in figure 6.10.

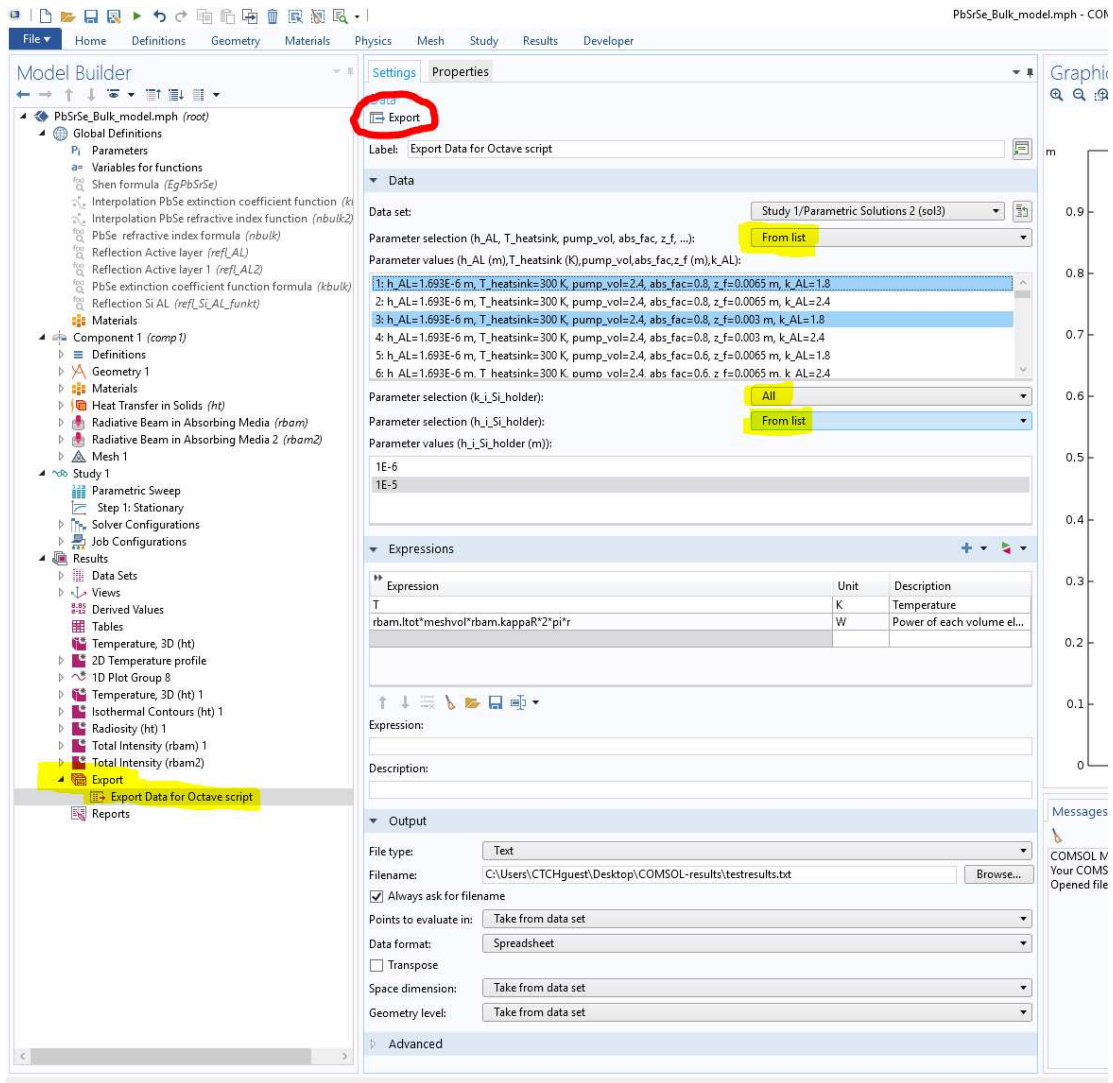


Figure 6.10: Data Export in the *COMSOL Multiphysics*<sup>®</sup> simulation model.

These files and the experimental data can now be used in the Octave script. Under the first section in the Octave script “USER INPUT” the parameters, legends and file names have to be adapted. Then the adapted script can be started to plot a comparison of the simulated and measured emission spectrum.

## 7 Results and Discussion

Several plots that have been generated by the beforehand explained procedure in *COMSOL Multiphysics*<sup>®</sup> simulation model and the following post processing in the Octave script will be shown. For that the thicknesses of the measured (and also simulated) chips are presented again:

Chip number	1832	1787	1738
Thickness of active layer	0.7 $\mu\text{m}$	1.2 $\mu\text{m}$	1.7 $\mu\text{m}$
Sr content	0%	0%	0%

A plot explanation will be given by having a look at the first plot 7.1:

- The upper left legend's 3 boxes:
  - plot 'number': 'heat sink temperature' K, 'pump laser power, in' V
  - 'chip number' 'heat sink temperature' K 'distance to focus point'  $\mu\text{m}$  with 'T\_0 for' the luminescence function, see formula (11)
  - Heatsink correction: value for horizontal shift of total spectrum in 'wavenumber'  $\text{cm}^{-1}$  / 'temperature' K
- The upper right legend informs about the 4 differently colored simulation results and it's thermal conductivities in [W/mK], which is the only varying parameter for this comparison plot. The last black line is the measured experimental data.
- The vertical colored lines and their temperatures in the graph inform about the maximum simulated chip temperature and its converted (via Shens band gap formula) wavenumber.
- The grey colored zone in the plot shows us the  $\text{CO}_2$  absorption to see its impact more clearly.

The measurements of the three mentioned chips were compared to their corresponding simulation results to find the unknown open parameters:

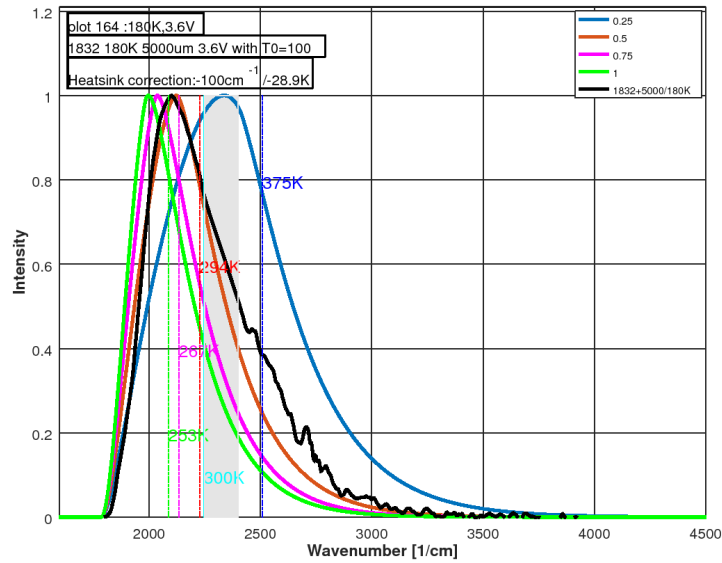


Figure 7.1: Comparison plot of simulation results for four different thermal conductivities with the corresponding measurement for chip 1832 at heat sink temperature = 180K, distance to focus point = 5 mm and with pump laser voltage = 3.6V

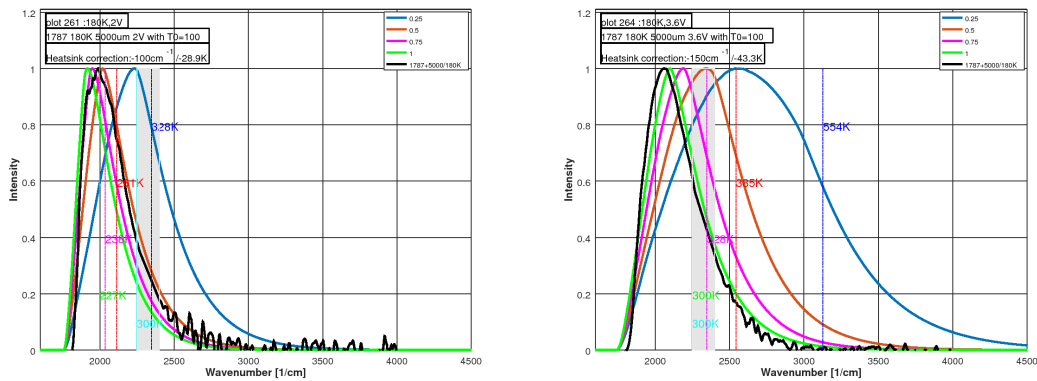


Figure 7.2: Comparison plot of simulation results for four different thermal conductivities with the corresponding measurement for chip 1787: left plot at heat sink temperature = 180K, distance to focus point = 5 mm and with pump laser voltage = 2.0V. Right plot at heat sink temperature = 180K, distance to focus point = 5 mm and with pump laser voltage = 3.6V

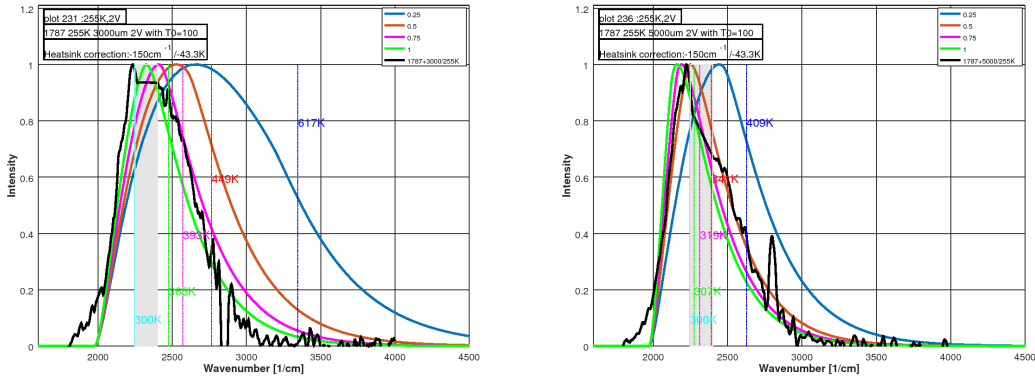


Figure 7.3: Comparison plot of simulation results for four different thermal conductivities with the corresponding measurement for chip 1787: left plot at heat sink temperature = 255K, distance to focus point = 3 mm and with pump laser voltage = 2.0V. Right plot at heat sink temperature = 255K, distance to focus point = 5 mm and with pump laser voltage = 2.0V

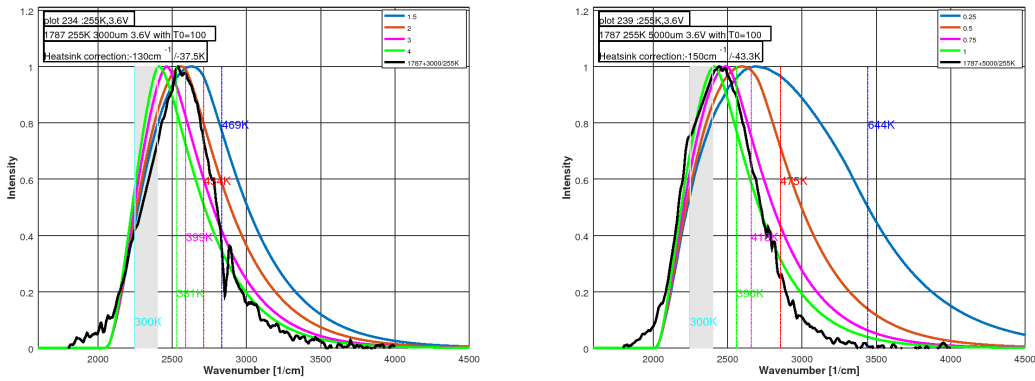


Figure 7.4: Comparison plot of simulation results for four different thermal conductivities with the corresponding measurement for chip 1787: left plot at heat sink temperature = 255K, distance to focus point = 3 mm and with pump laser voltage = 3.6V. Right plot at heat sink temperature = 255K, distance to focus point = 5 mm and with pump laser voltage = 3.6V

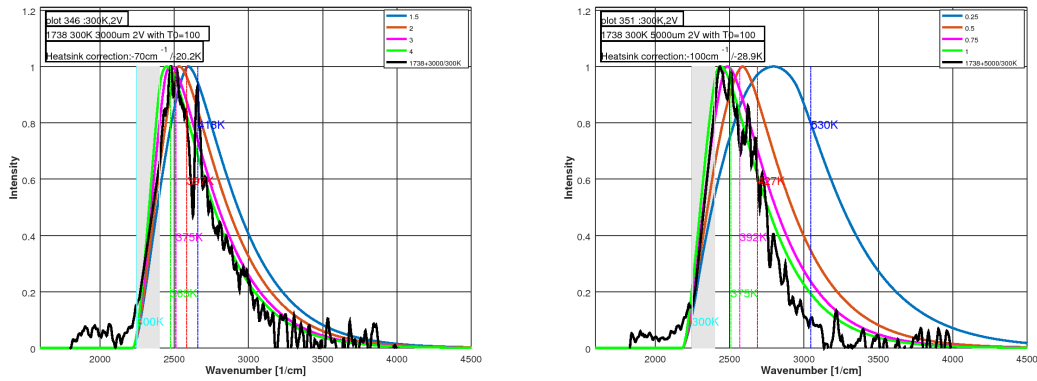


Figure 7.5: Comparison plot of simulation results for four different thermal conductivities with the corresponding measurement for chip 1738: left plot at heat sink temperature = 300K, distance to focus point = 3 mm and with pump laser voltage = 2.0V. Right plot at heat sink temperature = 300K, distance to focus point = 5 mm and with pump laser voltage = 2.0V

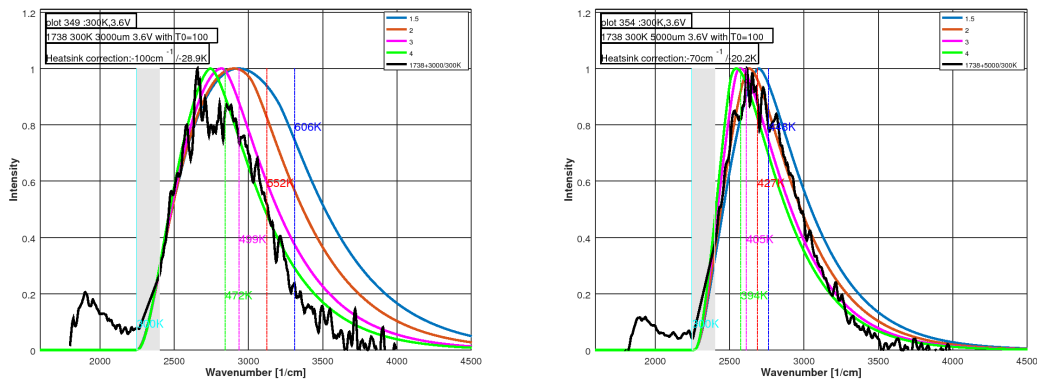


Figure 7.6: Comparison plot of simulation results for four different thermal conductivities with the corresponding measurement for chip 1738: left plot at heat sink temperature = 300K, distance to focus point = 3 mm and with pump laser voltage = 3.6V. Right plot at heat sink temperature = 300K, distance to focus point = 5 mm and with pump laser voltage = 3.6V

The presented plots are just a few of the  $\approx 150$  measured emission spectra, where each of them has been compared with eight different simulation results for thermal

conductivity and correction of heat sink temperatures. Three parameters were unknown and have to be found out by comparing to measurements:

- $T_0$  for the temperature dependent luminescence function, see formula (11).
- Thermal conductivity of PbSe active layer.
- Heat sink correction value for horizontal shift of total spectrum.

After looking through these comparison plots,  $T_0 = 100K$  was set as a constant for the temperature dependent luminescence function (formula 11).

To understand the behavior of the other two unknown parameters the simulation parameters pump laser power (=pump laser voltage) and distance to focus point were put together to a calculated pump laser intensity. It raises with higher pump laser power and lower distance to focus point.

We used that new summarized parameter intensity to understand overall trends by the following diagrams:

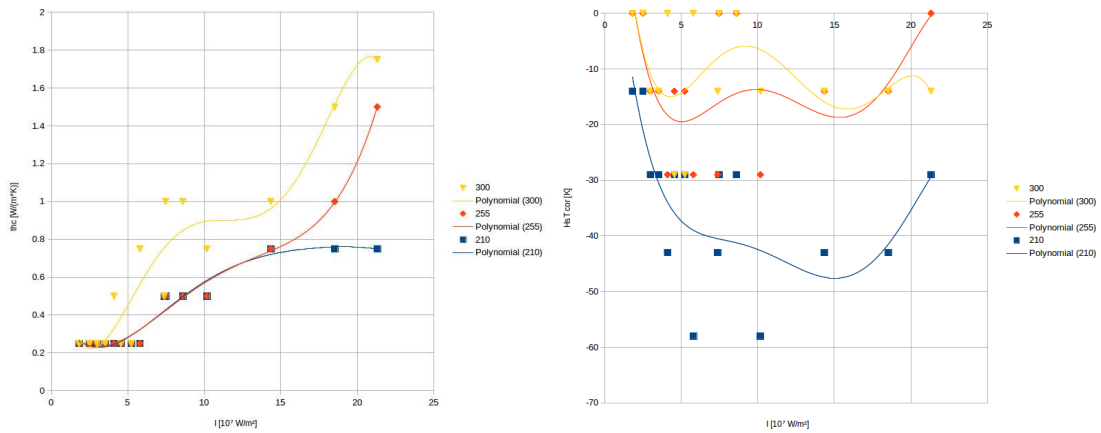


Figure 7.7: Overall trends displayed for the 1832 chip by diagrams at heat sink temperatures 210K, 255K & 300K in left: thermal conductivity vs pump laser intensity, right: heat sink correction vs pump laser intensity.

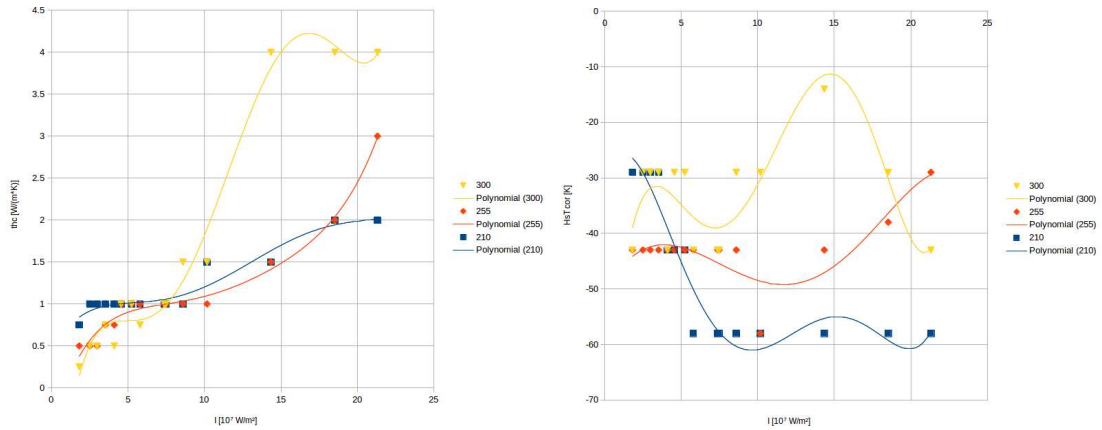


Figure 7.8: Overall trends displayed for the 1787 chip by diagrams at heat sink temperatures 210K, 255K & 300K in left: thermal conductivity vs pump laser intensity, right: heat sink correction vs pump laser intensity.

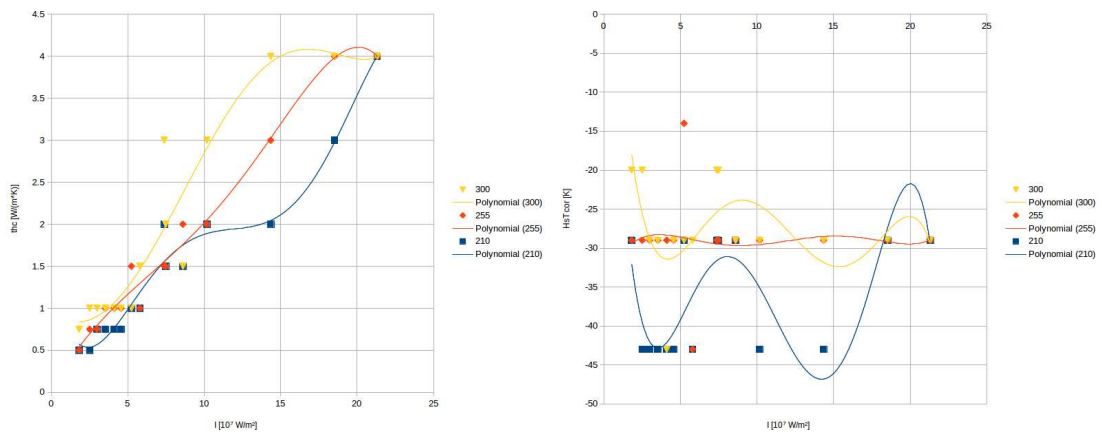


Figure 7.9: Overall trends displayed for the 1738 chip by diagrams at heat sink temperatures 210K, 255K & 300K in left: thermal conductivity vs pump laser intensity, right: heat sink correction vs pump laser intensity.

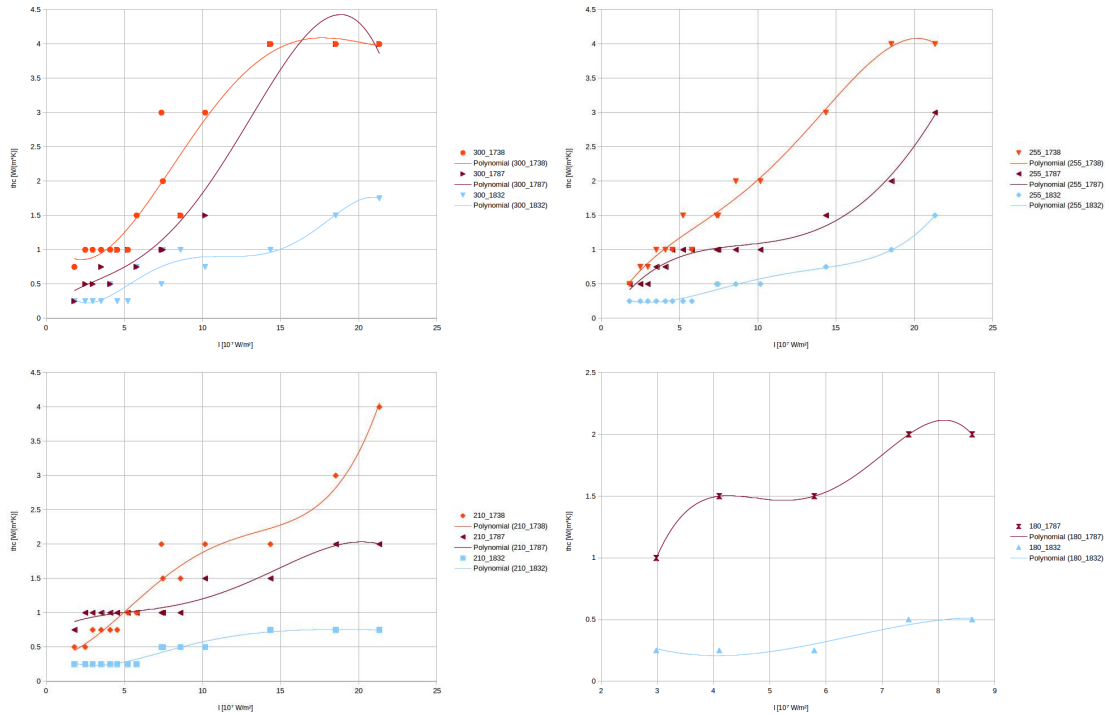


Figure 7.10: Overall trends summarized for all three chips into one thermal conductivity vs pump laser intensity diagram for each heat sink temperature: 300K (upper left), 255K (upper right), 210K (bottom left) & 180K (bottom right).

We concluded that thermal conductivity of the active layer raises with

- pump laser intensity
- heat sink temperature
- thickness of active layer

We also suspected similar behavior for the value maximum simulated chip temperature ( $=T_{max}$ ) - heat sink correction ( $=HsT_{cor}$ ) and therefore checked that with the following diagrams:

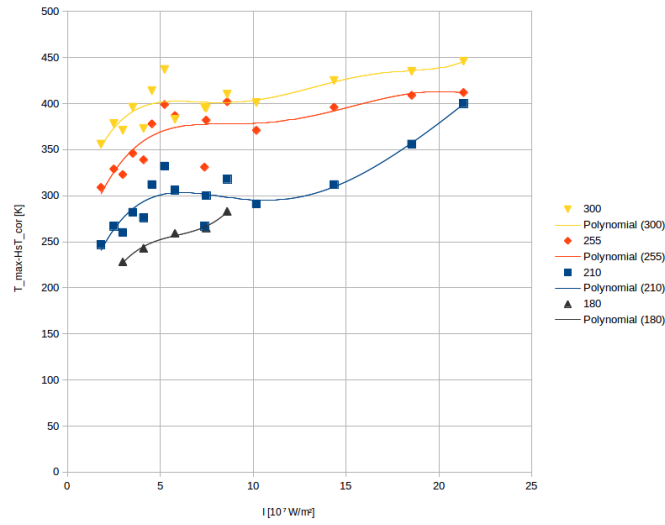


Figure 7.11: Overall trends of chip 1832 in a  $T_{max} - HsT_{cor}$  vs pump laser intensity diagram for heat sink temperatures: 300K, 255K, 210K & 180K.

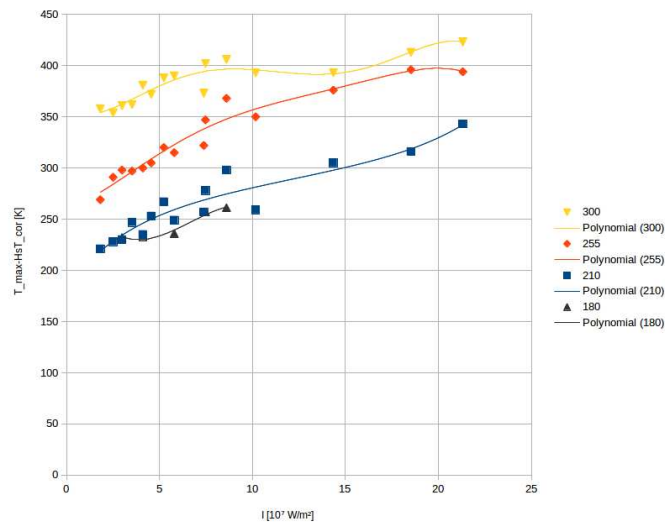


Figure 7.12: Overall trends of chip 1787 in a  $T_{max} - HsT_{cor}$  vs pump laser intensity diagram for heat sink temperatures: 300K, 255K, 210K & 180K.

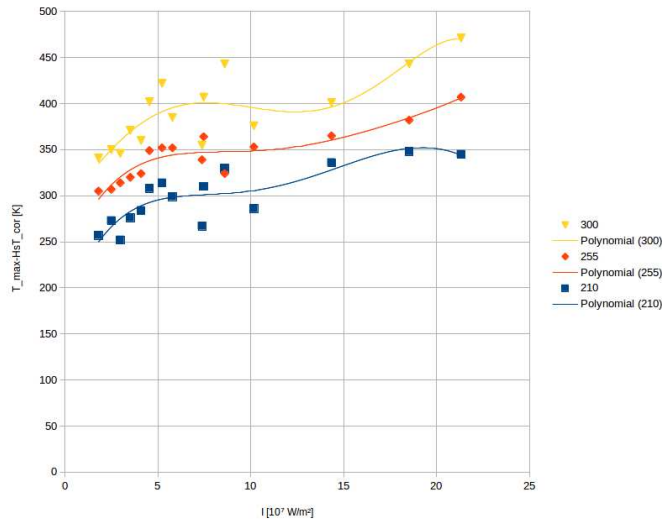


Figure 7.13: Overall trends of chip 1738 in a  $T_{\text{max}} - HsT_{\text{cor}}$  vs pump laser intensity diagram for heat sink temperatures: 300K, 255K & 210K.

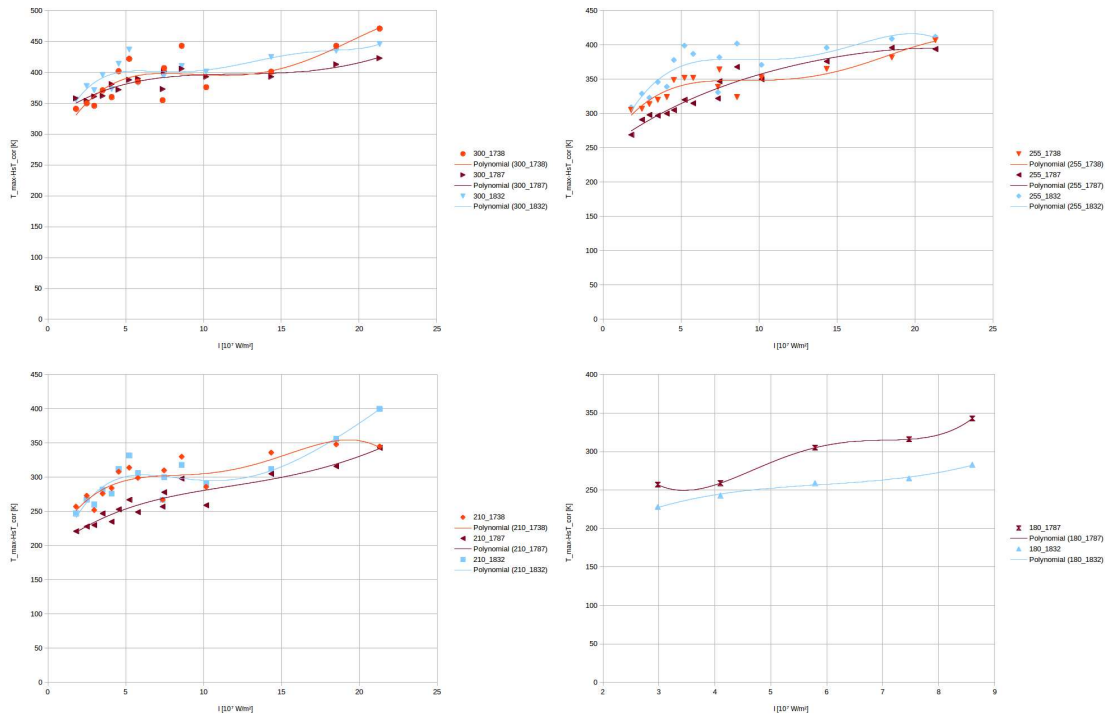


Figure 7.14: Overall trends summarized for all chips in one  $T_{\text{max}} - HsT_{\text{cor}}$  vs pump laser intensity diagram for each heat sink temperature: 300K (upper left), 255K (upper right), 210K (bottom left) & 180K (bottom right).

We concluded that the thermal conductivity can not be a constant value since it also changes under laser irradiation as it has also been measured in [JNC<sup>+</sup>11]. Therefore we decided to set the heat sink correction to a constant value and implement a thermal conductivity function that uses the measurement data as basis and depends on the above mentioned parameters in the listing (7). This thermal conductivity function does not represent a pure value for thermal conductivity, it is more like a function that sums up several occurring effects while the active layer is under laser irradiation.

This function is implemented in our *COMSOL Multiphysics*<sup>®</sup> simulation model for the more important reflection mode. It should generally work with PbSrSe-Bulk samples too, but that needs to be tested. For transmission mode, we assume that a scaling factors should make the function usable as well. Currently a constant value of 2.2 W/mK is set in the current simulation model. The following plots are the final simulation vs measurement results that only depend on the setup parameters:

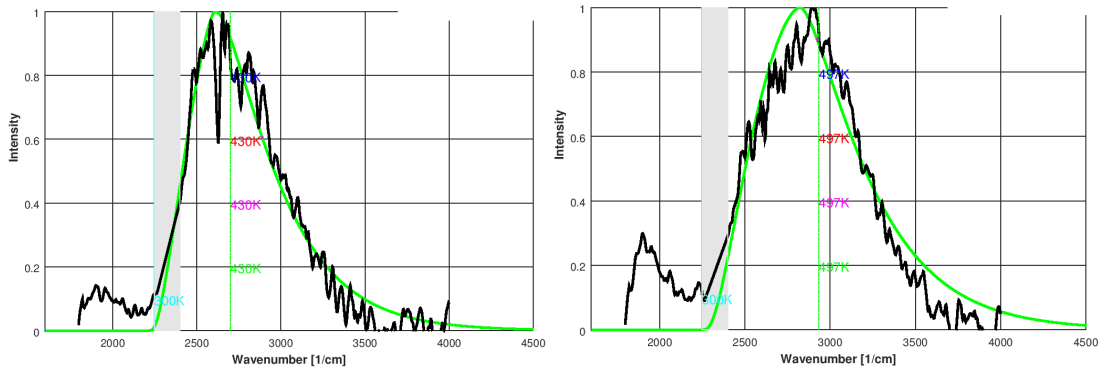


Figure 7.15: Final comparison plot of simulated emission (green) vs measured emission (black) for chip 1738 at heat sink temperature = 300K, distance from focus point = 3mm and for pump laser voltages left: 3V, right: 4V

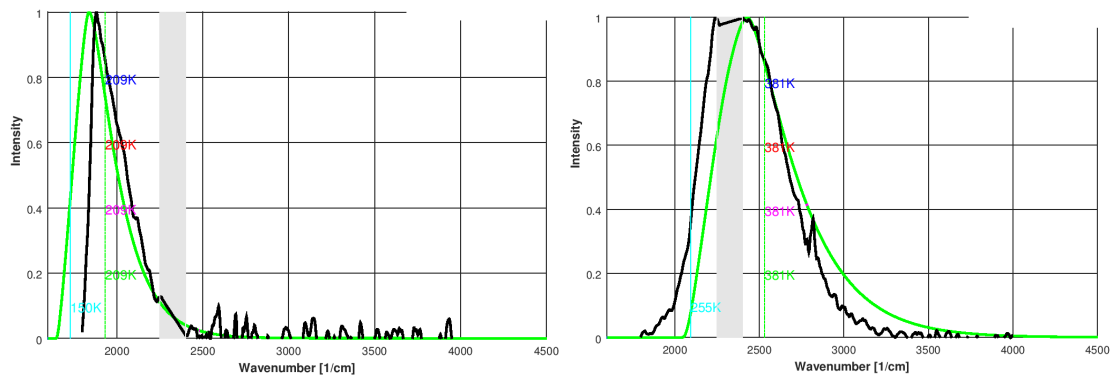


Figure 7.16: Final comparison plot of simulated emission (green) vs measured emission (black) for left: chip 1832 at heat sink temperature = 150K, distance from focus point = 6.5mm and for pump laser voltage = 2V. Note here that the detector cut off is at  $1800\text{ cm}^{-1}$  and therefore has a severe inaccuracy around that value.  
 right: chip 1787 at heat sink temperature = 255K, distance from focus point = 5mm and for pump laser voltage = 3V. Note here that the  $\text{CO}_2$  absorption zone is around the spectrum's peak and therefore influences its broadness greatly.

## 8 Conclusion and Outlook

The whole simulation with its model in *COMSOL Multiphysics*<sup>®</sup> and the script in Octave can be used to simulate a desired emission spectrum within minutes. Therefore it is useful to test assumptions before the lengthy production of a new chip is started. Solving the heat management problem will also be easier with this model. For example changing the sizes of the geometry or choosing different materials for the holder could already show a strong improvement towards better heat transfer.

Of course, there is also still room for improvement:

- A better understanding on how the thermal conductivity changes under laser irradiation would improve the results. [JNC<sup>+</sup>11] already provides some hints.
- Also a better understanding on how the refractive index changes under lasing conditions, as [SRK85] already mentions, could help. The interface reflection should be angle dependent in reflection mode.
- The whole setup with its surrounding could be build into the simulation. For example, the walls of the cryostat chamber radiate heat and could effect the chips heat transfer or simulate a more realistic heat sink cooling (we assumed constant heat sink temperature).
- For other not PbSe bulk chips, only the material and its properties (thermal conductivity, absorption coefficient, ...) have to be changed.
- For quantum well chips, most of the adaption have to be done in the Octave script by implementing the right calculation.
- A better understanding of the interface properties could also lead to more accurate results.

## References

- [And77] W Anderson. Gain-frequency-current relation for  $\text{Pb}_{1-x}\text{Sn}_x\text{Te}$  double heterostructure lasers. *IEEE Journal of Quantum Electronics*, 13(7):532–543, 1977.
- [BJF02] Peter W Bryce, Peter Jax, and Jie Fang. Leak-detection system designed to catch slow leaks in offshore Alaska line. *Oil & gas journal*, 100(50):53–59, 2002.
- [BRL<sup>+</sup>10] A Bauer, K Rößner, T Lehnhardt, M Kamp, S Höfling, L Worschech, and A Forchel. Mid-infrared semiconductor heterostructure lasers for gas sensing applications. *Semiconductor Science and Technology*, 26(1):014032, 2010.
- [CBJ12] James J Coleman, A Catrina Bryce, and Chennupati Jagadish. *Advances in semiconductor lasers*, volume 86. Academic Press, 2012.
- [com] <https://www.comsol.com/products>.
- [CS10] Wee Chew and Paul Sharratt. Trends in process analytical technology. *Analytical Methods*, 2(10):1412–1438, 2010.
- [DMS66] J. O. Dimmock, I. Melngailis, and A. J. Strauss. Band Structure and Laser Action in  $\text{Pb}_x\text{Sn}_{1-x}\text{Te}$ . *Phys. Rev. Lett.*, 16:1193–1196, Jun 1966.
- [FGE<sup>+</sup>95] ME Flatté, CH Grein, H Ehrenreich, RH Miles, and H Cruz. Theoretical performance limits of 2.1–4.1  $\mu\text{m}$  InAs/InGaSb, HgCdTe, and InGaAsSb lasers. *Journal of applied physics*, 78(7):4552–4559, 1995.
- [Fil11] Matthias Fill. *PbSe quantum well based mid-infrared vertical surface emitting lasers on silicon*. PhD thesis, ETH Zurich, 2011.
- [FPK<sup>+</sup>98] PC Findlay, CR Pidgeon, R Kotitschke, A Hollingworth, BN Murdin, CJGM Langerak, AFG van Der Meer, CM Ciesla, J Oswald, A Homer, et al. Auger recombination dynamics of lead salts under picosecond free-electron-laser excitation. *Physical Review B*, 58(19):12908, 1998.

- [GFH<sup>+</sup>06] Xiaoming Gao, Hong Fan, Teng Huang, Xia Wang, Jian Bao, Xiaoyun Li, Wei Huang, and Weijun Zhang. Natural gas pipeline leak detector based on NIR diode laser absorption spectroscopy. *Spectrochimica Acta Part A: Molecular and Biomolecular Spectroscopy*, 65(1):133–138, 2006.
- [IJC88] James D Ingle Jr and Stanley R Crouch. *Spectrochemical analysis*. Englewood Cliffs, N.J. : Prentice Hall, c1988, 1988.
- [Jef13] James D Jeffers. *Thermal conductivity measurements of IV-VI semiconductor nanostructures*. PhD thesis, University of Oklahoma, 2013.
- [JNC<sup>+</sup>11] James D Jeffers, Khosrow Namjou, Zhihua Cai, Patrick J McCann, and Leonard Olona. Cross-plane thermal conductivity of a pbsnse/pbse superlattice material. *Applied Physics Letters*, 99(4):041903, 2011.
- [Khi14] Amir Khiar. *Lead chalcogenide mid-infrared vertical external cavity surface emitting lasers*. PhD thesis, JKU Linz, 2014.
- [Kri07] Anthony Krier. *Mid-infrared semiconductor optoelectronics*, volume 118. Springer, 2007.
- [NS83] G Nimtz and B Schlicht. Narrow-gap lead salts. In *Narrow-Gap Semiconductors*, pages 1–117. Springer, 1983.
- [Pre79] H Preier. Recent advances in lead-chalcogenide diode lasers. *Applied physics*, 20(3):189–206, 1979.
- [PTC87] DL Partin, CM Thrush, and BM Clemens. Lead strontium telluride and lead barium telluride grown by molecular-beam epitaxy. *Journal of Vacuum Science & Technology B: Microelectronics Processing and Phenomena*, 5(3):686–689, 1987.
- [PV12] Ivan Pelant and Jan Valenta. *Luminescence spectroscopy of semiconductors*. Oxford University Press, 2012.
- [Rav03] Yu I Ravich. Lead chalcogenides: Basic physical features. *New York, Taylor and Francis. Redfield, AG (1957). " On the theory of relaxation*

processes." *IBM Journal of Research and Development*, 1(1):19–31, 2003.

- [RFFS14] Julien M Rey, Matthias Fill, Ferdinand Felder, and Markus W Sigrist. Broadly tunable mid-infrared vecsel for multiple components hydrocarbon gas sensing. *Applied Physics B*, 117(3):935–939, 2014.
- [RKF<sup>+</sup>09] M Rahim, A Khair, F Felder, M Fill, and H Zogg. 4.5  $\mu\text{m}$  wavelength vertical external cavity surface emitting laser operating above room temperature. *Applied Physics Letters*, 94(20):201112, 2009.
- [SJS<sup>+</sup>04] Steven W Sharpe, Timothy J Johnson, Robert L Sams, Pamela M Chu, George C Rhoderick, and Patricia A Johnson. Gas-phase databases for quantitative infrared spectroscopy. *Applied spectroscopy*, 58(12):1452–1461, 2004.
- [SJWW02] WZ Shen, LF Jiang, K Wang, and HZ Wu. Spectroscopic line shape broadening mechanisms in pbse/pbsrse quantum wells. *Journal of applied physics*, 91(10):6507–6510, 2002.
- [SRK85] YOSI Shani, RELI Rosman, and ABRAHAM Katzir. Calculation of the refractive indexes of lead chalcogenide salts and its application for injection lasers. *IEEE journal of quantum electronics*, 21(1):51–62, 1985.
- [SSA95] Norihiro Suzuki, Katsuyuki Sawai, and Sadao Adachi. Optical properties of pbse. *Journal of applied physics*, 77(3):1249–1255, 1995.
- [SYJ<sup>+</sup>02] WZ Shen, HF Yang, LF Jiang, K Wang, G Yu, HZ Wu, and PJ McCann. Band gaps, effective masses and refractive indices of pbsrse thin films: Key properties for mid-infrared optoelectronic device applications. *Journal of applied physics*, 91(1):192–198, 2002.
- [TACL71] TE Thompson, Paul Rs Aron, BS Chandrasekhar, and DN Langenberg. Magnetostriction and Magnetoelastic Quantum Oscillations in p- PbTe. *Physical Review B*, 4(2):518, 1971.

- [TC67] RN Tauber and IB Cadoff. Thermal and Optical Energy Gaps in  $\text{Pb}_{0.93}\text{Sn}_{0.07}\text{Te}$  and  $\text{Pb}_{0.85}\text{Sn}_{0.15}\text{Te}$ . *Journal of Applied Physics*, 38(9), 1967.
- [WFS<sup>+</sup>07] Christoph Walther, Milan Fischer, Giacomo Scalari, Romain Terazzi, Nicolas Hoyler, and Jérôme Faist. Quantum cascade lasers operating from 1.2 to 1.6 THz. *Applied Physics Letters*, 91(13):131122, 2007.
- [YKSB93] Shu Yuan, H Krenn, G Springholz, and G Bauer. Dispersion of absorption and refractive index of  $\text{PbTe}$  and  $\text{Pb}_{1-x}\text{Eu}_x\text{Te}$  ( $x < 0.05$ ) below and above the fundamental gap. *Physical Review B*, 47(12):7213, 1993.
- [YSP02] HF Yang, WZ Shen, and QJ Pang. Study of optical constants in pbsrse thin films for mid-infrared laser application. *Journal of Physics: Condensed Matter*, 14(8):2067, 2002.
- [ZRC<sup>+</sup>09] SY Zhang, DG Revin, JW Cockburn, K Kennedy, AB Krysa, and M Hopkinson.  $\lambda \sim 3.1\mu\text{m}$  room temperature  $\text{InGaAs/AlAsSb/InP}$  quantum cascade lasers. *Applied Physics Letters*, 94(3):031106, 2009.